Torkjell Stenvold

Offshore Gravimetric and Subsidence Monitoring

Thesis for the degree philosophiae doctor

Trondheim, June 2008

Norwegian University of Science and Technology
Faculty of Engieering Science and Technology
Department of Petroleum Engineering and Applied Geophysics

NTNU

NTNU
Norwegian University of Science and Technology

Thesis for the degree philosophiae doctor

Faculty of Engieering Science and Technology
Department of Petroleum Engineering and Applied Geophysics

ISBN 978-82-471-1046-1 (printed version)
ISBN 978-82-471-1047-8 (electronic version)
ISSN 1503-8181

Doctoral theses at NTNU, 2008:183

Printed by NTNU-trykk

Acknowledgements

I thank my advisors Ola Eiken (StatoilHydro) and Martin Landrø (NTNU) for good advice and support during my work on this thesis. I also thank Håvard Alnes, Scott Nooner, Glenn Sasagawa, and Mark Zumberge which together with Ola and me comprise the core personnel that have planned and carried out the surveys as well as interpreted and presented the data acquired. Without their help I would not have completed this thesis. Thanks go to Patrick Walsh and Jose Otero who have worked on the ROVDOG and helped perform the surveys since 2005. Jon Lippard helped carry out the 2007 Snøhvit survey. Thanks also go to the anonymous reviewers of the SPE Journal paper (Chapter 2). I finally thank Statoil for financing my PhD.

Table of contents

1 Introduction

In order to optimize production and the recovery of hydrocarbon fields it is necessary to monitor reservoir fluid flow. This is conventionally done by monitoring well production and injection rates, various well pressure measurements, well tests, and well logging. Tracers may be used to monitor inter-well flow, and reservoir geophysics may be used to monitor field-wide reservoir flow. Time-lapse (4D) seismic is now probably the most well-known and wide spread geophysical reservoir monitoring technique. Its success in identifying in-fill (undrained) targets at the Gullfaks oilfield (Landrø et al. 1999) and other influential results and arguments (e.g. Jack 1997), have helped make it an established reservoir surveillance technique in major oil companies like StatoilHydro, Shell, and BP (Foster 2008).

In short one may say geophysical monitoring is used to enhance the description and understanding of reservoir flow so that the costs of monitoring are more than covered by improved recovery or smarter production or both. It may also be viewed as a way to reduce risk associated with events like undrained segments or excessive water influx. To get full benefit of monitoring programs, some intervention capacity (like ability to redirect old wells, drill new wells, and handle water production) should be catered for. With the high oil and gas prices of today combined with few new significant hydrocarbon discoveries, new and improved techniques for reservoir monitoring are probably more relevant than ever. Furthermore, under the intimidating threat of global warming, CO_2 storage is likely to become wide-spread, and methods to monitor such storage sites will presumably be welcomed.

Given the mass changes above and below the reservoir are negligible (or correctable), gravimetric fieldwide monitoring can provide a reservoir density change map (Chapter 1.1). The largest and most rapid density changes are associated with fluids of different density displacing each other. The potential bulk density change also depends on porosity and residual (irreducible) fluid saturations (Chapter 8.4). A significant fluid density contrast occurs when water displaces gas (like water influx or injection into gas reservoirs or gas caps), when gas displaces water (e.g. CO_2 injection into aquifers), and when gas displaces oil (gas injection or gas cap expansion). Reservoir thickness and reservoir depth are also important factors for the feasibility of gravimetric monitoring (Chapter 8.3).

Water influx can significantly affect the production and recovery of gas fields (Agarwal et al. 1965). Gravimetric monitoring can in principle both map and quantify water influx, and may thus help gas reservoir management. Knowledge of the water influx strength can be important for if and when a compressor for lowering the abandonment pressure is required, and for determining the optimal production rate. As discussed in Chapter 8, the mapping of water influx can be particularly useful for offshore gas fields where well coverage is usually sparse and wells are expensive; e.g. if a well is choked off by water it is of interest to know if this is a local occurrence and perhaps also where it is safe to drill new wells.

Sparse well data not only implies uncertainty about the distribution of encroaching water, it also implies uncertainty about the amount of water encroached. Given there is no water influx or contact movement detected from the wells, then water can only be inferred indirectly by pressure data and some form of material balance. The problem is that in principle this is a non-unique problem even for a homogenous reservoir/aquifer system (unless the active gas in place is exactly known, which it never is). Bruns et al. (1965) warned that a straight line in the P/Z-plot of the material balance (see equation 8.6 for the P/Z formula) not necessarily means

the reservoir is volumetric (i.e. zero water influx), and that whether the *P*/*Z*-curve is linear or not will depend on the aquifer influx function (as well as on the production rate). A typical mistake is to assume a volumetric reservoir and extrapolate the apparently linear *P*/*Z*-curve to get the gas in place *G* on the abscissa. If the reservoir is energized by water influx, such an approach will give a too large estimate of *G* (Bruns et al. 1965). The error is easy to make early in a field's life because sometimes as much as half the gas in place needs to be produced before the *P*/*Z* plot start showing the upward concave shape (theoretically it may never show up) diagnostic of water influx. To complicate things further, a concave downward shape has been reported for reservoirs where there is a significant pressure gradient across the water flooded zone (Cason 1989). Cason shows an example where the early-time straight-line *P*/*Z* persisted until 40 to 50 % of *G* was produced, which could have resulted in overestimating *G* by 25 to 50 % if extrapolated.

Because reservoir fluid production and injection data are measured and presented in volumes, it is useful to roughly quantify the minimum water volume detectable by gravity data for a given reservoir. For local water influx we can use the point mass formula or equivalently the formula of a sphere (Telford et al 1990, p. 35) to estimate the minimum required water influx volume δW_e to give a detectable gravity signal. Assuming the gas takeout effect is compensated for or negligible (see Chapter 8 for more on this effect), the minimum detectable water influx volume is approximated by

$$\delta W_e = \frac{z^2 \delta \Delta g}{G \Delta \rho_f}, \tag{1.1}$$

where $\delta\Delta g$ is the gravity detectability, $\Delta\rho_f$ is the density contrast between gas and water, z is the vertical depth to the point mass (or equivalently to the centre of a sphere of equivalent mass and density $\Delta\rho_f$), and $G = 6.672 \times 10^{-3}$ μGal m^2/kg is the Newtonian constant. If we for a single observation point use $\delta\Delta g = 10$ μGal (like in Chapter 8.3) and $\Delta\rho_f = 850$ kg/m^3, then for a reservoir depth $z = 1000$ m the minimum detectable water volume is $\delta W_e = 1.8 \times 10^6$ m^3. For twice the depth, $z = 2000$ m, $\delta W_e = 7.1 \times 10^6$ m^3. In comparison, the movable gas volume for the Dake example of Table 8-2 (p. 131) is 77×10^6 m^3, while for the Troll field it is about 4×10^9 m^3.

Time-lapse seismic can also be used to monitor gas reservoirs. For typical reservoir depths being in the kilometre range, time-lapse seismic has usually lateral resolution an order of magnitude better than the gravity method. For migrated 3D seismic, half the seismic wavelength is used as a rule of thumb for lateral resolution (Brown 2004, p. 6); theoretically, perfect migration can reduce the width of the Fresnel zone and thus the lateral resolution to a quarter of a wavelength (Lindsey 1989). The seismic wavelength is seismic velocity v divided by the dominant frequency f. Values for a reservoir at more than 2 km depth can be $f = 25$ Hz and $v = 2500$ m/s, giving a lateral resolution of about 50 m (using the half-wavelength criterion). In comparison, the lateral resolution of the gravity method is in the order of reservoir depth. Regarding vertical resolution, Alsos et al (2003) found (using seismic time-lapse tuning) a detection threshold of 9 m rise in gas water contact for the Sleipner Øst field. This is impressive considering the reservoir depth is about 2400 m below sea level. However, seismic does not provide unambiguous density information, and the velocity dependence on saturation is not really known (patchy vs. Gassmann relation, see Figure 5-4). There may also be cases where the acoustic impedance contrast is too low compared to the 4D seismic noise level to be distinguished; the non-repeatable noise can be significantly higher than expected if the weather is bad during data acquisition, e.g. due to streamer repositioning errors. Gravimetric monitoring can give unambiguous density change information (and total mass

change), and when averaged over a larger area it can give better vertical resolution than the 4D seismic: as seen in Chapter 9, the vertical resolution is 8 m for a horizontal disk of radius 1.2 km at 2.3 km depth given (observed) time-lapse uncertainty of 3.6 μGal. Thus time-lapse gravity and time-lapse seismic are complementary techniques which together may put stronger constraints on the reservoir flow model than if used alone.

Subsidence data from seafloor pressure measurements (measured together with gravity) is usually more sensitive to reservoir pressure change than gravity (Chapter 1.3), and thus offers complementary information. Relative depth changes are also needed for correcting the jointly measured gravity changes for height changes. Subsidence data can be used to estimate reservoir compaction, from which inferences about reservoir pressure or reservoir compressibility can be made (Chapter 1.2). To keep track of subsidence can be important for the safety of wells and offshore installations (Chapter 2.2). Field-wide subsidence measurements can improve geomechanical models, and may thus also improve the description of reservoir fluid flow for cases when flow and deformation is coupled. The methodology and results of using seafloor water pressure measurements for subsidence monitoring are covered in Chapter 2. It appears to me that this is the most accurate technique available to monitor large areas offshore for subsidence: on Troll 1.0 cm is the observed scatter for the time-lapse depth differences between 2002 and 2005 after a weak subsidence signal is removed (Chapter 4.4.2). Note that on Troll only 20-30 % of the stations were visited more than once in each of the surveys, and the distances between the stationary reference pressure stations were in the range 16-26 km. If all stations are visited at least twice in both surveys and the distances between the reference pressure stations are reduced to e.g. 10 km, then a time-lapse accuracy of 0.5 cm should be feasible. Echo-sounding has been used to map seafloor subsidence on Ekofisk (Nagel 2001), where it has put important constraints on the geomechanical field-wide modelling and the overburden in particular (Nagel 1998). On Ekofisk, subsidence of nearly 8 m had been observed by year 2000 (Chin and Nagel 2004). However, the relative depth accuracy of echo-sounding (Hammerstad 1997) appears to be more than an order of magnitude worse (decimetre range) than for the pressure method.

Onshore, time-lapse gravity has been used to monitor geothermal fields (Chapter 1.4), water storage aquifers (Davis et al. 2005), volcanoes and magma chambers (Chapter 1.4), and mining subsidence (Lyness 1985). Applications to gravity variations associated with tectonic processes (intra- and inter-plate), postglacial isostatic rebound, and deep mass movements in mantle and core, are covered in Torge (1989). The monitoring of other hydrocarbon fields (Gröningen and Prudhoe Bay) is briefly discussed in Chapter 8.2.

Gravimetric and subsidence monitoring of offshore hydrocarbon fields is a new method patented by Eiken et al. (2003). A brief history of this technique follows. In the mid 90ties Ola Eiken worked as a Statoil geophysicist on the giant Troll East gas field which was to be put on stream in 1996. It was while thinking on possible ways to monitor this areally extensive field he got the idea that time-lapse gravimetry could be a suitable method. He found that there was no commercially available gravimetric technique sufficiently accurate to monitor offshore hydrocarbon fields; e.g. is ship gravimeter accuracy in the 100 μGal range, which is more than the total potential time-lapse anomaly for most hydrocarbon fields. The solution thus appeared to be constrained to measurements on the seafloor. Although there had been examples of seafloor gravimeters used for research purposes (Chapter 3.2), no one had devised a method for the precise repositioning required for time-lapse work or with the required data acquisition efficiency. Ola Eiken got in contact with Mark Zumberge from Scripps Institution of Oceanography in 1996, an experienced geophysicist with specific

knowledge of gravimeters and oceanographic work. This was the start of the cooperation between Statoil and Scripps on gravimetric monitoring that is still ongoing. They came up with a solution of the repositioning problem, which involved: pressure gauges put together with the gravimeter(s) in a single instrument that could be carried by a ROV (Remotely Operated Vehicle), deployment of reference gauges for continuous pressure measurements, and deployment of permanent seafloor benchmarks (Chapter 3; Eiken et al. 2000). The use of pressure gauges turned out to be an accurate way of monitoring seafloor subsidence as well (Chapter 2), although it can be susceptible to benchmark movements at shallow water depths due to scouring (Chapter 2.5.8). Since no such instrument existed, they decided to build it themselves at Scripps (Chapter 3.3) and named it ROVDOG (Remotely Operated Vehicle Deep Ocean Gravimeter).

To measure gravity on the seafloor in the North Sea proved challenging due to unavoidable rough instrument handling and narrowband noise during measurement. The gravity repeatability of 26 μGal obtained in the first 1998 Troll survey was below expectations. To improve on this, the number of gravimeters in the ROVDOG was increased from 1 to 3 prior to the Troll 2000 survey. One other important change was the optimization of the calibration cycle for the CG-3 gravimeters with thought of the noisy seafloor environment (done by Håvard Alnes who worked as a summer student for Statoil in 2000); by default the gravity recording was originally interrupted for 1 s every 13th second (Chapter 3.3.2), which was the main reason for the periodic narrowband noise being quite slowly reduced by averaging at a rate of about $2\sqrt{N}$, where N is the number of seconds in the recording. For uninterrupted series the narrowband/background noise reduced approximately by a factor N, meaning that a 20 minutes record would reduce a 2 mGal rms noise to a couple of μGals. Still, the initial results of the 2000 survey did not live up to the expectations with an arithmetic average (of the three gravimeters) repeatability of 19 μGal (Table 3-2). The main problem was large recoveries (short term drift during measurements) and quite unpredictable survey drift. However, the better noise reduction allowed the recoveries to be better diagnosed. Later reprocessing with more weight on the best performing gravimeter, some recovery minimizing steps (like editing out the beginning of records), and a lower threshold for editing dubious measurements, improved the repeatability to 11 μGal (Table 4-1). Based on experience from the first two surveys and lab tests, what turned out to be major improvements to the instrument and procedures were made (Chapter 4). The main steps involved a better shock-protecting frame, an automatic levelling program to keep the gravimeters roughly centred during transport, more effort put into keeping the ambient temperature stable during surface transits, and revisiting of a base network station every 12h for better drift control. This led to a breakthrough for the Troll 2002 and Sleipner 2002 surveys where repeatabilities better than 4 μGal were obtained (Table 4-1). A point to notice is that hardly any records were discarded during processing of the Troll 2002 data (of the best unit only 4% of the records, which all were part of an un-closed loop, were discarded), which is in contrast to the 2000 survey where a fifth of the measurements of the best unit was discarded. Since the 2002 surveys the CG-3 gravity sensor cores have been replaced by CG-5 gravity sensor cores, a chiller unit is used to keep stable water bath temperature during surface transits, the sensitivity of the pressure gauges to rotations is corrected for, relative height corrections for benchmark tilt have been performed, and more care has been required for the gravimeter scale factor calibrations (Chapter 4). The 1/6 Hz sampling for the CG-5 gravimeters and no need of collecting calibration signals, seems to have increased the rate for which narrowband noise is reduced: now it appears to reduce quicker than N (where N is number of seconds in the recording) for the fields at around 300 m water depth (at more shallow depths, like Sleipner with its 80 m, there can be low frequent wave induced noise that is reduced slower).

Gravimetric and subsidence monitoring is currently used on six fields offshore Norway: Troll and Sleipner in the North Sea; Midgard, Mikkel, and Ormen Lange (field trial) in the Norwegian Sea; and Snøhvit in the Barents Sea. Some key statistics from these surveys are listed in Table 4-1 (page 64). We observe that the intra-survey repeatability has been improved from 26 μGal in 1998 to 3-5 μGal in recent surveys. This is as good as high quality microgravity surveys on land. Note that 1 μGal = 10^{-8} m/s^2. Relative depths are obtained with precision of typically 3-6 mm.

Both subsidence and time-lapse gravity (excluding borehole gravity) is surface map data that in principle, given the reservoir geometry is reasonably well known and the reservoir thickness is modest compared to reservoir depth, can be converted to a reservoir compaction map and a reservoir density change map, respectively. This conversion is essentially a 2D interpretation, and some basic theory and examples are reviewed in Chapters 1.1 and 1.2. As is seen in Chapter 1.2, subsidence data can be interpreted analogous to gravity data for linear elastic deformation in a homogenous media. In Chapter 1.3 the sensitivity of gravity, subsidence data, and seismic to reservoir pressure change is compared using real data available from Troll Øst. In volcanology and for geothermal fields, gravity monitoring and surface deformation data have been used for decades. These areas are briefly reviewed in Chapter 1.4.

1.1 2D gravity interpretation

The vertical component of gravity g_z due to a density distribution $\rho(\alpha,\beta,z)$ at a point (x,y,h) above the distribution is

$$g_z(x,y,h) = G\int_0^{\infty}\int_{-\infty}^{\infty}\int_{-\infty}^{\infty} \frac{\rho(\alpha,\beta,z)(z-h)}{\left\{(x-\alpha)^2+(y-\beta)^2+(z-h)^2\right\}^{3/2}}\mathrm{d}\alpha\mathrm{d}\beta\mathrm{d}z \qquad (1.2)$$

where (α,β,z) are the subsurface coordinates of an elemental mass unit, and G is the Newtonian gravitational constant. The depth z is positive downwards. It can be shown (Roy 1962) that for any point on or above the source distribution $\rho(\alpha,\beta,z)$, there exist a distribution of density per unit area σ on any plane or surface above the sources that will produce the same gravity anomaly as the real source distribution. Hence equation 1.2 can be written as

$$g_z(x,y,h) = G\int_{-\infty}^{\infty}\int_{-\infty}^{\infty} \frac{\sigma(\alpha,\beta,d)(d-h)}{\left\{(x-\alpha)^2+(y-\beta)^2+(d-h)^2\right\}^{3/2}}\mathrm{d}\alpha\mathrm{d}\beta \qquad (1.3)$$

where $\sigma(\alpha,\beta,d)$ is the areal density distribution of a plane at depth d, and is often termed the "equivalent source" (Dampney 1969) or "equivalent layer" (Leäo and Silva 1989).

The equivalence of equation 1.2 and 1.3 illustrates the ambiguity of surface gravity interpretation. The ambiguity was illustrated by Skeels (1947) who calculated sources in a plane that gave rise to the observed gravity anomaly. As noted by Roy (1962) it is obvious that a 3D distribution $\rho(\alpha,\beta,z)$ in general cannot be uniquely determined from a 2D distribution $g_z(x,y,h)$. What may be less obvious is that the equivalence also implies that $g_z(x,y,h)$ contains all the attainable information from above the sources; i.e. gradient data or

anomaly values at various heights do not provide independent information and can be computed from $g_z(x,y,h)$ (Roy 1962). However, in the real world with discrete data and noise, it is an advantage to measure as close as possible to the sources.

Roy (1962) noted that the concept of ambiguity in gravity interpretation appeared to be somewhat over-emphasized. Hence he gave three conditions under which equation 1.2 can be uniquely solved. The first is when the density variation is limited to a plane at a known depth $z = d$. Then the unknown function $\sigma(\alpha,\beta,d)$ is dependent on only two variables, and can therefore be determined by knowledge of $g_z(x,y,h)$ and solution of equation 1.3. The second condition is when the density contrast is a constant and its bounding surface has a known shape. The third condition is a generalization of the first, see Roy (1962) for details.

The first condition is in practice closely met for many reservoirs that are thin compared to their depth and for which negligible density changes occur below and above the reservoir. Then we can use the relation

$$\sigma(\alpha,\beta,d) = \overline{\rho}(\alpha,\beta,d)H(\alpha,\beta,d) \tag{1.4}$$

where H is reservoir thickness and $\overline{\rho}$ is the vertically averaged density over the reservoir thickness. I.e. equations 1.2, 1.3, and 1.4 practically hold at the same time. In other words, given σ (inverted from gravity data) and given H (usually from seismic and well data), the density (change) $\overline{\rho}$ can be uniquely determined. $\overline{\rho}(\alpha,\beta,d)$ then makes physical sense as a reservoir density change map. The further mapping to a change in gas water contact or in saturation requires knowledge of more parameters (Chapter 8.4).

Equation 1.3 is in the form of a 2D convolution integral, and can be written as

$$g_z(x,y,h) = \sigma(x,y,d) * K(x,y,d-h) \tag{1.5}$$

where * denotes convolution and

$$K(x,y,d-h) = \frac{G(d-h)}{\left\{x^2+y^2+(d-h)^2\right\}^{3/2}}. \tag{1.6}$$

The convolution theorem states that if two terms are convolved in the space domain then they are multiplied in the wavenumber domain (and vice versa)). Taking the Fourier Transform of both sides of equation 1.5 gives

$$\tilde{g}_z(k_x,k_y,h) = \tilde{\sigma}(k_x,k_y,d)\cdot\tilde{K}(k_x,k_y,d-h) \tag{1.7}$$

where k_x and k_y are the wavenumbers (spatial frequencies) corresponding to x and y, related by the Fourier Transform. The Fourier transform of the gravity distribution is

$$\tilde{g}_z(k_x,k_y,h) = \int_{-\infty}^{\infty}\int_{-\infty}^{\infty} g_z(x,y,h)e^{-i(k_x x+k_y y)}dxdy. \tag{1.8}$$

$\tilde{\sigma}(k_x,k_y,d)$ and $\tilde{K}(k_x,k_y,d-h)$ are similarly the Fourier Transforms of their space domain equivalents. Regarding the impulse response, $K(x,y,d-h)$, its Fourier Transform is (Blakely 1996, p. 273)

$$\tilde{K}(k_x,k_y,d-h) = 2\pi G e^{-(k_x^2+k_y^2)^{1/2}(d-h)}, \qquad d > h. \tag{1.9}$$

As an alternative to deconvolution, equation 1.5 can be solved by spectral division of equation 1.7 by equation 1.9 followed by an inverse Fourier Transform, i.e.

$$\sigma(x,y,d)=\frac{1}{2\pi}\int_{-\infty}^{\infty}\int_{-\infty}^{\infty}\tilde{g}_z(k_x,k_y,h)e^{i(k_x x+k_y y)}\frac{1}{2\pi G}e^{(k_x^2+k_y^2)^{1/2}(d-h)}dk_x dk_y\,. \tag{1.10}$$

Hence the inverse of equation 1.9

$$\tilde{K}^{-1}(k_x,k_y,d-h)=(2\pi G)^{-1}e^{(k_x^2+k_y^2)^{1/2}(d-h)}, \tag{1.11}$$

is often referred to as the inverse earth filter. Except for the constant G^{-1} equation 1.11 is equivalent to the operator used for downward continuation of the gravity field from *h* to *d* in the Fourier domain, i.e.

$$\tilde{g}_z(k_x,k_y,d)=(2\pi)^{-1}\tilde{g}_z(k_x,k_y,h)\cdot e^{(k_x^2+k_y^2)^{1/2}(d-h)}\,. \tag{1.12}$$

1.1.1 Discrete case

In practice the data is available at a finite number of discrete points and contains noise, while the model is infinite dimensional. Hence the problem can according to inverse theory be considered non-unique because there will exist an infinite number of models that can satisfy the data (Parker 1977). To make the problem unique, some form of model averaging or additional assumptions or both have to be made. However, this is difficult to do with a continuous model and use of functionals, so the common approach is to make the model discrete as well.

For the gravity 2D problem, it is plausible to discretize the reservoir map into a 2D grid. If the cell dimensions are less than about a fourth of the reservoir depth, the point mass formula can be used with little loss in accuracy (must be seen relative to noise level). Then the gravity change Δg_{ij} at station *i* caused by a density change $\Delta\rho_j$ in reservoir cell *j* is expressed as

$$\Delta g_{ij}=G\frac{z_{ij}\Delta\rho_j V_j}{\left(r_{ij}^2+z_{ij}^2\right)^{3/2}} \tag{1.13}$$

where z_{ij} is the vertical distance (depth), r_{ij} is the horizontal distance, V_j is the cell volume, and *G* is the Newtonian gravitational constant. For a larger cell size to depth ratio, the formula for a rectangular prism (Blakely 1996) or, for less regular cell geometry, the polyhedron formula may be used (Singh and Guptasarma 2001). Anyway, given the reservoir is thin compared to reservoir depth, the model density changes are linearly related to the observed gravity changes, and are conveniently expressed in matrix notation as

$$\Delta\mathbf{g}=\mathbf{A}\Delta\boldsymbol{\rho} \tag{1.14}$$

where $\Delta\boldsymbol{g}$ is the $m\times1$ gravity change vector, $\Delta\boldsymbol{\rho}$ is the $n\times1$ density change vector, and $\mathbf{A}$ is the $m\times n$ system matrix ($\mathbf{A}_{ij}=Gz_{ij}V_j\left(r_{ij}^2+z_{ij}^2\right)^{-3/2}$ if the point mass formula is used).

The origin of the rule of thumb criteria for lateral resolution (that it equals source depth) is not clear (it is often mentioned but never cited). One origin may be the shape of the anomaly due to a point source (equation 1.13): when the lateral distance between two positive point masses of equal strength equals the depth to the point masses, we get a resultant anomaly on the surface with practically flat top as seen in the upper left plot of Figure 1-1 (thick line), making the two individual sources practically inseparable. However, it is here more relevant to consider the resolution of two sources of different magnitude, the extreme case being two sources of opposite sign as illustrated in the right pane of Figure 1-1. Then it is no problem distinguishing the two sources situated a depth interval apart (top right plot), and even a smaller separation interval would be possible to discern.

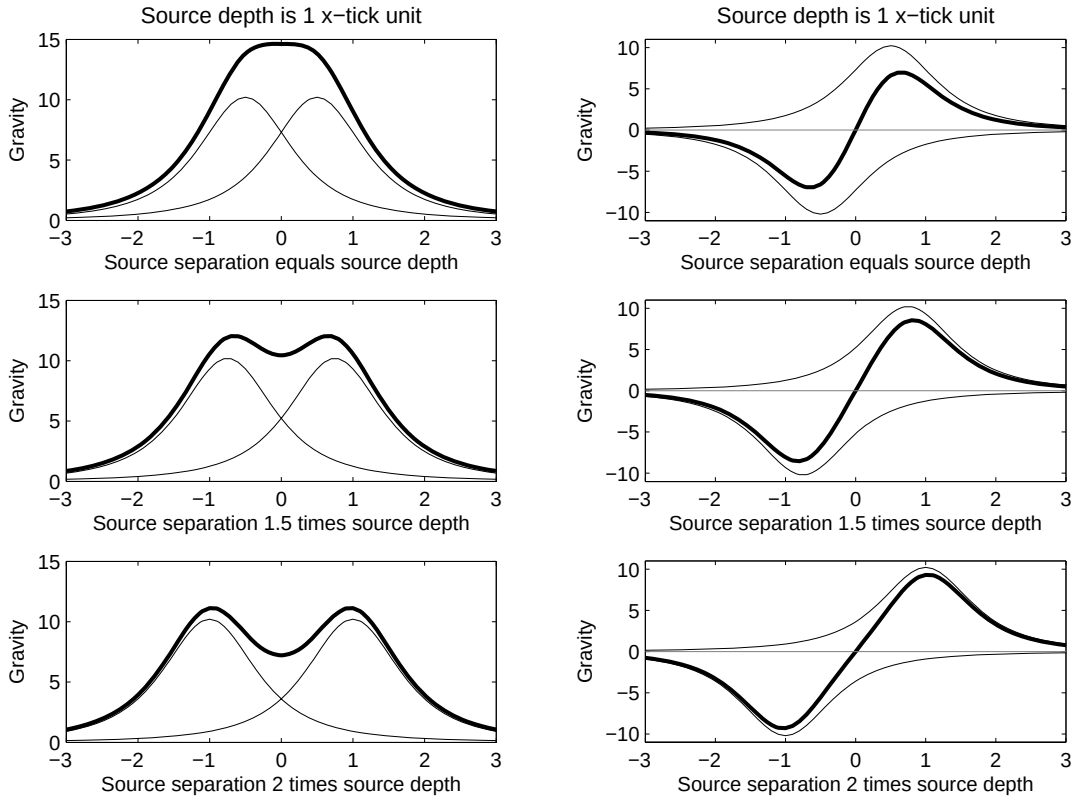

Figure 1-1: Gravity anomalies of two point sources placed at the same depth with three different lateral spacings. The resultant anomaly as would be observed on surface is drawn with thick line, while the two individual anomalies are drawn with thin lines. In the left panes the sources are positive and of equal strengths, and in the right panes the left source is negative and the right source is positive but with same strength. In the top plots the source spacing equals source depth, in the middle plots the source spacing is 1.5 times source depth, and in the bottom plots the source spacing is 2 times source depth

An overview of the effect of the signal to noise ratio and depth on lateral resolution is probably easiest seen in the Fourier domain. As seen from equation 1.11 the inverse filter grows exponentially with depth ($z = d - h > 0$) and with wavenumber $k = (k_x^2 + k_y^2)^{1/2}$.

Conversely are the amplitudes of the high wavenumbers in the source distribution exponentially attenuated with depth (equations 1.7 and 1.9). Because the spectrum of the ambient noise will tend to be fairly flat (if random), the naïve application of equation 1.10 (or its discrete equivalent) when the gravity data contains noise can lead to severe noise inflation. An impression of the lateral resolution for a given source distribution can be obtained by inspecting where the spectrum of its gravity anomaly intersects the flat noise spectrum. However, this gives an estimate of global resolution, not local resolution. This can be an important distinction because the resolution will vary with position dependent on the source strength distribution (given the noise distribution is spatially invariant).

From the above and because the gravity anomaly is a blurred/low-pass version of the mass distribution, caution is required when equation 1.14 is to be solved. In fact, the gravity inverse problem is to be regarded as a severely ill-posed problem, that is, it gets very unstable if too

much detail (resolution) is attempted. The traditional way to deal with such problems is some form of Tikhonov regularization (ridge regression) or truncated SVD. Such methods and their proper use are treated in Hansen (1998).

If more control is available or wanted on the individual model parameters, the bounded-variable least-squares (BVLS) algorithm derived by Stark and Parker (1995) is the method to use. In terms of equation 1.14, BVLS solves the problem

$$\min_{\rho_1 \le \Delta\rho \le \rho_2} \left\| \mathbf{A}\Delta\boldsymbol{\rho} - \Delta\mathbf{g} \right\|_2 \tag{1.15}$$

where $\boldsymbol{\rho}_1, \Delta\boldsymbol{\rho}, \boldsymbol{\rho}_2 \in \mathbf{R}^{\mathbf{n}}$, $\Delta\boldsymbol{g} \in \mathbf{R}^{\mathbf{m}}$, and $\mathbf{A}$ is the $m \times n$ matrix. The relative size of m and n is immaterial, i.e. the algorithm can be used even when $m << n$ (strongly underdetermined problem). Stark and Parker also show how to use the BVLS algorithm to solve the related minimum 1-norm and ∞-norm problems, and how a misfit constraint can be added to the parameter constraints (bounded-variable misfit). Regarding the 2D gravity problem, one should be a little careful putting too strict constraints on the densities, as there can be significant uncertainty in the reservoir thickness map away from wells (as well as in porosities and residual saturations). It is not uncommon that 4D seismic interpretation has led to a new structural interpretation as well, e.g. due to the top reservoir reflector being weak and difficult to track on the base seismic survey.

1.2 Subsidence interpretation

In order to interpret subsidence caused by reservoir depletion, it can be useful to first consider the basic case valid for linear elastic deformations with no elastic contrast between the reservoir and the surrounding rock (infinite homogenous half-space). For this case, by use of the theory of linear poroelasticity (Wang 2000), subsidence can be explicitly related to reservoir depletion in terms of a few parameters (equation 1.16). By the principle of superposition, estimates of field-wide subsidence can be easily attained if a sufficiently finely gridded reservoir thickness (isocor) map is available (equation 1.22), which is considerably less time consuming than setting up a full-field finite-element model. An advantage of having a elementary model which is derived from a definite physical concept, is that it can serve as a basis for interpretation of more advanced models: e.g. do Morita et al. (1989) use finite element modelling to investigate the impact of a contrast in elastic properties between the reservoir and the surrounding rock, and Merle et al. (1976) report on how the use of a rigid basement makes the subsidence anomaly sharper and of higher peak amplitude. The elementary model may also be use to investigate when a more advanced model is required (Bruno 2002).

For a homogenous and linear elastic halfspace with a traction free horizontal surface, the surface vertical strain (subsidence) caused by the shrinkage or compaction of an inclusion of volume V (nucleus of strain with small but finite volume) is (Geertsma 1973)

$$S(r,0) = -\frac{1}{\pi} C_m (1-\nu) \frac{D}{(r^2 + D^2)^{3/2}} \Delta P \cdot V \tag{1.16}$$

where C_m is the uniaxial compressibility (zero lateral strains), ν is the Poisson's ratio ($-1 > \nu \geq 0.5$), D is the depth to V, r is the horizontal distance to V, and ΔP is the pressure depletion of V. The ratio of surface horizontal strain to subsidence is $-r/D$. Interestingly, equation 1.16 is of the same form as the gravity impulse response given in equation 1.6. Hence the discussion in the previous section regarding gravity interpretation is highly relevant for subsidence data as well.

When the reservoir lateral dimensions are large compared to its thickness, the reservoir deforms predominantly in the vertical plane (Geertsma 1973); i.e. reservoir compaction or a reduction in reservoir volume is primarily a result of a reduction in reservoir height (~zero lateral strains). The uniaxial compressibility can then be estimated by

$$C_m = \frac{1}{\Delta P}\frac{\Delta h}{h} \tag{1.17}$$

where h is reservoir height and $\Delta h = h_2 - h_1$ is reservoir compaction. From equation 1.16 and 1.17 we observe that Δh in principle can be uniquely inferred from subsidence data given ν is known. Since Δh equals the product $h\,C_m \Delta P$, a-priori knowledge of two out of these three product terms is required for a unique determination.

The uniaxial compressibility is related to rock bulk compressibility C_b (inverse of bulk modulus) by

$$C_m = \frac{1}{3}\left(\frac{1+\nu}{1-\nu}\right)\left(1 - C_r/C_b\right)C_b, \tag{1.18}$$

where C_r is the rock matrix compressibility (Geertsma 1973). When $C_r << C_b$, equation 1.18 simplifies to

$$C_m = \frac{1}{3}\left(\frac{1+\nu}{1-\nu}\right)C_b = \frac{1}{M}, \tag{1.19}$$

i.e. C_m then equals the inverse of the plane wave (P-wave) modulus M. Fjær et al. (2008, p. 394) discuss the proper use of M in association with sonic and seismic data. Note that Fjær et al. (2008, p. 393) use equation 1.19 to define C_m, and hence use $\Delta h/h = C_m\left(1 - C_r/C_b\right)\Delta P$ instead of equation 1.17; the term $\left(1 - C_r/C_b\right)$ is called the Biot coefficient.

Under uniaxial conditions and when $C_r << C_b$, we can express C_m in terms of the (uniaxial) pore compressibility C_p and porosity ϕ by

$$C_m \cong \phi C_p\,. \tag{1.20}$$

Equation 1.16 follows the principle of superposition. Given a reservoir grid of m cells we can thus estimate the subsidence S_j at a surface or seafloor station j by

$$S_j = -\frac{1}{\pi}C_m(1-\nu)\sum_{i=1}^{m}\frac{D_{ij}}{(r_{ij}^2 + D_{ij}^2)^{3/2}}\Delta P_i \cdot V_i\,. \tag{1.21}$$

The subsidence at the n seafloor stations can be conveniently expressed by the matrix multiplication

$$\mathbf{s} = \mathbf{A}\mathbf{x}, \tag{1.22}$$

where $\mathbf{s}$ is the $n\times 1$ subsidence vector, $\mathbf{x}$ is the $m\times 1$ model vector ($x_i = C_m(1-\nu)\Delta P_i \cdot V_i$), and $\mathbf{A}$ is the $n\times m$ system matrix ($\mathbf{A}_{ij} = -\pi^{-1}D_{ij}(r_{ij}^2 + D_{ij}^2)^{-3/2}$). For the match of observed subsidence with modelled subsidence in Chapter 2.6 it was the product $C_m(1-\nu)$ that was solved for, and C_m was estimated assuming $\nu = 0.25$.

It is sometimes argued that for real deformations due to pressure depletion there will be irreversible and nonlinear components, and thus the linear poroelastic approach is too simplistic. According to Bruno (2002) the elastic overburden deformation assumption is

usually valid; e.g. even for a severe formation compation of 10 m and given a relative shallow depth of 1000 m, the strains over the 1000 m overburden thickness will maximum be 1 % (and usually much less) and the elastic material assumptions will be usually accurate. Bruno states that for a given amount of subsurface compaction, resulting surface subsidence is relatively insensitive to overburden material properties, so that analytical nucleus of strain equations provide good subsidence approximations to even sophisticated geomechanical models which account for inelastic and heterogeneous overburden behavior (within about 20%); more sophisticated models are usually only required to account for the formation compaction itself or to accurately evaluate deformations and stresses in the overburden (e.g. to assess casing damage risk).

Quite recent examples of inversion of subsidence data for reservoir deformation associated with hydrocarbon fields are given by Marchina (1996), Vasco et al. (2000), Du and Olson (2001), and Fokker (2002). Common to their approaches is that they use some form of penalized least squares for the solution of their respective version of equation 1.22.

Vasco and Feretti (2005) show that when the reservoir behaves poroelastically, flow properties such as permeability can be inferred from reservoir volume change derived from surface displacement data or time-lapse seismic. However, Xu and Nur (2001) show for a synthetic square reservoir example that boundary effects (open or closed to flow) can give a quite similar pressure depletion response as permeability anisotropy. They also warn against solely using subsidence data to infer reservoir boundaries, as an elongated subsidence bowl does not always mean the reservoir is actually elongate, but could be caused by permeability anisotropy or reservoir boundaries.

Interferometric (satellite) Synthetic Aperature (InSAR) is a onshore subsidence monitoring technique that deserves special mention because of its large areal coverage, quite high resolution (grid cells of typically 30x30 m), high accuracy (1 cm or even 1 mm of surface deformation), frequent updates (depends on the satellite orbit time and coverage), and relatively low cost (Xu and Nur 2001). As stated by Vasco et al. (2002), InSAR has been used to map topography, to image displacements induced by earthquakes, to image deformation associated with magmatic systems, and to image ice dynamics; InSAR has also proved useful in observing subsidence associated with mining, geothermal production, petroleum production, and aquifer compaction (Vasco et al. 2002). The subsidence accuracy of InSAR can be degraded by temporal changes in e.g. vegetation (Vasco and Feretti 2005).

1.3 Pressure sensitivity comparison of time-lapse gravity, subsidence data, and 4D seismic

Given the uncertainty of time-lapse gravity data, subsidence data, and 4D seismic timeshifts, the sensitivity to a reservoir pressure change is here investigated. For the 4D seismic and the subsidence data, observed sensitivities to pressure from Troll East are used; for the gravity data the in comparison well-known theoretical sensitivity to pressure is used (negligible fluid substitution is assumed). The combination of Troll East being an areally extensive field (area ~416 km^2) with a shallow reservoir depth of ~1.2 km below the seafloor and a presumably fairly uniform reservoir pressure drop, means the 1D-formulas (see below) can be used with fairly good accuracy to describe the pressure sensitivity of gravity and subsidence data. This gives these methods a slightly too good pressure sensitivity because the 1-D formulas can be seen to represent the maximum vertical detectability limit (Chapter 8.3). On the other hand is

the observed uncertainty of 1 cm for the subsidence data and 6.5 μGal for the time-lapse gravity data likely to be at least a factor $\sqrt{2}$ worse than what is expected between recent and future surveys (e.g. Midgard and Mikkel) due to instrument improvements and more repeat measurements (Table 4-1).

The gravity 1D response due to pure pressure depletion (no saturation change) is found by combining equation 8.2 and 8.4 to

$$\Delta g_{1D} = 2\pi G Ntg \cdot \phi S_{g1} \rho_{g1} C_g h \Delta P \,. \tag{1.23}$$

Here the pore compressibility was assumed negligible compared to the gas compressibility. Inserting into equation 1.23 the value for the gravitational constant (G = 6.672 ×10^{-3} μGal m^2/kg), a Net-gross-ratio Ntg = 0.95, a porosity ϕ = 0.3, a gas saturation S_{g1} = 0.7, a gas density ρ_{g1} = 113 kg/m^3, a gas compressibility C_g = 6.5x10^{-3} bar^{-1}, and a reservoir thickness h = 100 m, gives a gravity sensitivity to pressure of 0.61 μGal/bar.

The pressure sensitivity or uncertainty given a gravity uncertainty (standard deviation) of $\delta\Delta g$ is

$$\delta\Delta P = \left(2\pi G Ntg\, \phi S_{g1} \rho_{g1} C_g h\right)^{-1} \delta\Delta g \,. \tag{1.24}$$

For $\delta\Delta g$ = 6.5 μGal, which is the time-lapse gravity uncertainty on Troll (Table 4-2), $\delta\Delta P$ = (6.5 μGal)/0.61 μGal/bar) = 10.6 bar.

The 1D response of subsidence to reservoir compaction C to subsidence S is found from equation 1.16 (in a similar manner as the gravity Bouguer response is derived) to be

$$S_{1D} = -2(1-\nu) C_m h \Delta P = -2(1-\nu)\Delta h \tag{1.25}$$

where C_m is the uniaxial reservoir compressibility, and h is the reservoir thickness. It is interesting and surprising (to me) to note that equation 1.25 implies that the volume of the subsidence bowl will be larger (-1 < ν < 0.5) or equal to (ν = 0.5) the volume of reservoir compaction for this model (also observed by Fjær et al. 2008, p. 405). Inserting C_m = 1.8×10^{-5} bar^{-1} (Chapter 7.5), ν = 0.25 (was used in the inversion for C_m, so its value does not affect the sensitivity), and h = 100 m, gives a subsidence sensitivity to pressure of 0.27 cm/bar.

The pressure sensitivity or uncertainty given a subsidence uncertainty (standard deviation) of δS is

$$\delta\Delta P = \left[2(1-\nu) C_m h\right]^{-1} \delta S \tag{1.26}$$

For δS = 1.0 cm, which is the subsidence uncertainty on Troll (Chapter 4.4.2, the "height changes" section), $\delta\Delta P$ = (1.0 cm)/0.27 cm/bar) = 3.7 bar.

For the Troll East reservoir, Eiken and Tøndel (2005) found a linear correlation between seismic time-shift Δt and reservoir thickness h between 1997 and 2002, expressed as

$$\Delta t = 2\alpha h \Delta P / u + const \,, \tag{1.27}$$

where u = 2400 m/s is the compressional seismic velocity and α = 5×10^{-4} bar^{-1} is the derived pressure sensitivity. Here I use equation 1.27 with $const$ = 0. Inserting these values and h = 100 m, gives a seismic time-shift sensitivity to pressure of 0.042 ms/bar.

The pressure sensitivity or uncertainty given a time-shift uncertainty (standard deviation) of $\delta\Delta t$ is

$$\delta\Delta P = u\left(2\alpha h\right)^{-1} \delta\Delta t \tag{1.28}$$

According to Eiken and Tøndel (2005) the timing uncertainty $\delta\Delta t$ is 0.1-0.2 ms dependent upon the degree of spatial smoothing applied. If we use 0.1 ms, $\delta\Delta P$ = (0.1 ms)/0.042 ms/bar) = 2.4 bar.

From the above results time-lapse seismic appears to be most sensitive to a pressure change. It is 3.7/2.4 = 1.5 times more sensitive than subsidence data and 10.6/2.4 = 4.4 times more sensitive than the gravity data. Hence the vertical resolution of seismic and subsidence data to a reservoir pressure change is fairly similar on Troll.

The three methods are sensitive to different parameters for a given pressure change, which can be illustrated by dividing the changes by each other. Such ratios reveal which parameters are likely to be better determined by joint inversion methods. E.g. by dividing equation 1.25 by equation 1.23 and inserting equation 1.20 we get

$$\frac{\Delta h}{\Delta g} = \frac{-2(1-\nu)\phi C_p h \Delta P}{2\pi G Ntg\, \phi S_{g1}\rho_{g1} C_g h \Delta P} = \frac{-(1-\nu)C_p}{\pi G Ntg\, S_{g1}\rho_{g1} C_g}. \tag{1.29}$$

This holds for both the 1D case and for the general point-source case, but requires negligible water influx and that the simple homogenous subsidence model is reasonably valid.

1.4 Geothermal fields and volcanology

Geothermal fields are used to produce electricity, and in the process large amounts of hot water or steam are extracted, and sometimes water is re-injected. Annual gravity changes up to 100 μGal have been observed at the Wairakei geothermal Field (Hunt 1970). Hunt (1970) used Gauss's potential theorem (Hammer 1945) on the measured gravity changes to calculate net mass loss (i.e. mass withdrawn – mass recharge). Allis and Hunt (1986) contributed to the use of gravimetric monitoring for interpretation by relating the mass changes to physical changes in the reservoir, like changes in pressure, temperature and saturation. They also emphasized the importance of having a precise base survey prior to production, the essential requisite (for land surveys) of field-wide and regular measurements of groundwater levels by shallow wells, and the potential benefits of extending subsidence and gravity surveys well beyond the known or inferred field boundaries. The last point is in my opinion not so critical for hydrocarbon fields when the reservoir geometry (or at least its horizontal extent) is well known.

Hunt and Kissling (1994) summed up how gravity monitoring at the Wairakei and Ohaaki geothermal fields up to then had been used to: determine fluid recharge over the whole field, estimate changes in saturation in the steam zone in different parts of the field, check the validity of numerical reservoir simulation models for exploitation, and to determine the path of re-injected fluid. From their study they found that when the rate of mass transfer is controlled by the reservoir permeability, the analysis of gravity changes can also give inferences about permeability, permeability-thickness and storativity.

At the Bulalo geothermal field fieldwide gravity monitoring enabled the location of subsurface mass withdrawals to be mapped without any drillhole information, and provided an independent constraint on reservoir modeling of steam saturation changes over time and space (San Andres and Pedersen 1993). Nordquist et al. (2004) report on the important role gravity monitoring has played in refining the latest reservoir simulation model, which has

resulted in a simulation model that more accurately reflects natural recharge patterns and better predicts reserves and future reservoir performance. They emphasize that internal flow effects in most of the wells rendered their pressure and temperature measurements uncertain and not necessarily representative for static reservoir values. Hence gravity data became particularly important for calibrating the net depletion of the numerical model and for constraining reservoir mass replacement from reinjection and natural inflow from aquifers outside the production zone.

In volcanology, combined surface deformation and gravity change measurements have been frequently used to estimate magma chamber volume and mass changes, respectively. Together these measurements can give density change estimates important for the interpretation of magma movements, and may thus ultimately lead to better prediction of volcanic eruptions (Rymer 1993; Williams-Jones and Rymer 2002). Continuous gravity measurements have also been used (e.g. Berrino et al. 2006), and in association with such investigations papers on the behaviour of the CG-3 Scintrex gravimeters have been published (Bonvalot et al. 1998; Carbone and Rymer 1999). An example of how discrete and continuous gravity observations can be used together to get a more complete picture of the spatial and temporal characteristics of volcanic processes is given by Carbone et al. (2003). Nooner (2005) gives a good review of the literature on the use of gravity change measurements and deformation measurements within volcanology and other areas as well.

1.5 Organization of the thesis

The introduction (Chapter 1) is complemented by the introductions given in Chapters 2 to 8. I am the first author of the articles in chapter 2 and 8. For the 5 articles in between I am a co-author, and the sum of my contributions to those articles (as quantified by the respective first authors) represents about one article.

Chapter 2 contains the article “High-precision relative depth and subsidence mapping from seafloor water-pressure measurements” by Stenvold et al. (2006), published in the *SPE Journal*. It was submitted in March 2005, and a revised version that also contained results from the Troll 2005 survey (August) was submitted in February 2006. The method of obtaining high-precision relative depth measurements by the use of mobile pressure gauges is presented. Intra-survey and inter-survey depth repeatabilities from six surveys are presented, and the individual contributing errors are discussed and estimated. Average reservoir compressibility for the Troll field between 2002 and 2005 is obtained by matching measured subsidence with modeled subsidence.

Chapter 3 contains the article “A new seafloor gravimeter” by Sasagawa et al. (2003), published in *Geophysics*. It was submitted in September 2001, and a revised version was submitted in August 2002. This article describes the ROVDOG (Remotely operated Vehicle-deployed Deep-Ocean Gravimeter) in detail. Gravity and pressure repeatability results from the two first Troll surveys in 1998 and 2000 are presented. Data reduction, instrumental and environmental corrections are also presented.

Chapter 4 contains the article “Precision of seafloor gravity and pressure measurements for reservoir monitoring” by Zumberge et al., and was submitted 29 February 2008 to *Geophysics*. This builds on the article by Sasagawa et al. (Chapter 3). Improvements and up-to date intra- and inter survey repeatability results are presented. The emphasis is on gravity

results since the relative depth measurements are discussed in Stenvold et al. (Chapter 2). A latitude dependence of the calibration scale factors of Scintrex gravimeters is shown for the first time.

Chapter 5 contains the article "Constraints on the in situ density of CO_2 within the Utsira formation from time-lapse seafloor gravity measurements" by Nooner et al. (2007), published in the *International Journal of Greenhouse Gas Control*. In this article gravity measurements made on 30 seafloor stations above the CO_2 bubble in 2002 and 2005 have been used to constrain the in-situ density of CO_2 for models derived from seismic. The gravity responses of various numerical models are compared for the1999 to 2001 period. Note that time-lapse seismic for the 2002-2005 period was not available when this article was written.

Chapter 6 contains the article "Monitoring both gas production and CO_2 injection at the Sleipner field using time-lapse gravimetry" by Alnes et al., submitted 29 February 2008 to *Geophysics*. This is a renewed analysis of the same gravity data as in the article by Nooner et al. (Chapter 5). Recently available 4D seismic, a more updated reservoir simulation model, and reprocessed gravity and pressure data give a new estimate of CO_2 density. The observed gravity response between 2002 and 2005 from the underlying Ty Formation is shown for the first time.

Chapter 7 contains the article "Gravimetric monitoring of gas production from the Troll field" by Eiken et al., submitted 3 April 2008 to *Geophysics*. The gravity data is used to map and quantify water influx on Troll between 2002 and 2005. There is good agreement with well data and the amount of water influx agrees with material balance calculations.

Chapter 8 contains the article "Gravimetric monitoring of gas reservoir water influx—a combined flow- and gravity-modeling approach" by Stenvold et al., and was accepted for publication in January 2008 by *Geophysics*. It is to appear in an upcoming special section on 4D gravity monitoring. The vertical resolution for a given gravity detectability has been quantified in terms of the height of a vertical cylinder model, and is expressed in terms of cylinder density and cylinder radius to depth ratio. Gravity modeling is combined with the reservoir engineering techniques of material balance, aquifer influx functions, and front displacement angle. Hence the gravity response of edge water or basal water influx can be quickly evaluated for various gas production rates and aquifer strengths (given linear reservoir geometry). Edge water influx is found to be detectable at early stages.

In Chapter 9 some closing remarks regarding gravity monitoring are made. For similar remarks regarding the pressure measurements and subsidence monitoring, see Chapter 2.7

Chapter 2

High-Precision Relative Depth and Subsidence Mapping From Seafloor Water-Pressure Measurements

Is not included due to copyright

Chapeter 3

A new seafloor gravimeter

Is not included due to copyright

Chapter 4

Precision of seafloor gravity and pressure measurements for reservoir monitoring

Is not included due to copyright

5 Constraints on the in situ density of CO2 within the Utsira formation from time-lapse seafloor gravity measurements

Scott L. Nooner[1,*], Ola Eiken[2], Christian Hermanrud[2], Glenn S. Sasagawa[1], Torkjell Stenvold[3], Mark A. Zumberge[1].

[1]Scripps Institution of Oceanography, University of California San Diego, La Jolla, CA 92093, United States
[2]Statoil Research Centre, Rotvoll, N-7005 Trondheim, Norway.
[3]The Norwegian University of Science and Technology (NTNU), N-7491, Trondheim, Norway

[*]Corresponding author at: Lamont-Doherty Earth Observatory, Columbia University, Palisades, NY 10964, United States.

5.1 Abstract

At Sleipner, CO_2 is being separated from natural gas and injected into an underground saline aquifer for environmental purposes. Uncertainty in the aquifer temperature leads to uncertainty in the *in situ* density of CO_2. In this study, gravity measurements were made over the injection site in 2002 and 2005 on top of 30 concrete benchmarks on the seafloor in order to constrain the in situ CO2 density. The gravity measurements have a repeatability of 4.3 μGal for 2002 and 3.5 μGal for 2005. The resulting time-lapse uncertainty is 5.3 μGal. Unexpected benchmark motions due to local sediment scouring contribute to the uncertainty. Forward gravity models are calculated based on both 3D seismic data and reservoir simulation models. The time-lapse gravity observations best fit a high temperature forward model based on the time-lapse 3D seismics, suggesting that the average in situ CO_2 density is about to 530 kg/m^3. Uncertainty in determining the average density is estimated to be ±65 kg/m^3 (95% confidence), however, this does not include uncertainties in the modeling. Additional seismic surveys and future gravity measurements will put better constraints on the CO_2 density and continue to map out the CO_2 flow.

5.2 Introduction

5.2.1 The Sleipner Project

The Sleipner Project is the world's first commercial application of emissions avoidance through the use of carbon capture and sequestration technologies for geologic storage of CO_2. The Sleipner field is a natural gas production area located about 240 km off the coast of Norway in the North Sea (Figure 5-1) and operated by Statoil. In order for natural gas drawn from the site to meet commercial specifications, its CO_2 content must be reduced from about 9 to 2.5%. In gas fields worldwide, this excess CO_2 is typically vented into the atmosphere,

but at Sleipner the CO_2 is compressed and injected into a porous saline aquifer known as the Utsira formation (Figure 5-2). Injection began in 1996; now about 1 million tonnes (MT) of CO_2 are being separated from the natural gas and injected into the Utsira formation each year.

Because this is the first industrial-scale project of CO_2 injection into a geologic formation for environmental sequestration, monitoring the CO_2 is useful in confirming that this is a safe and reliable sequestration option. Previously, time-lapse 3D seismic surveys have been successfully employed to image the underground CO_2 (Arts et al., 2003; Chadwick et al., 2004).

Figure 5-1: A map of the southern Norwegian coastline. The location of the Sleipner platform is indicated by a square in the lower left corner of the map.

In this study, we obtain seafloor gravity measurements in 2002 and 2005. We also construct a series of gravity forward models using the results from both the seismic surveys and reservoir simulation models that were computed by the independent research company SINTEF. These are used to help interpret changes in gravity from 2002 to 2005 in order to place bounds on the in situ density of CO_2.

5.2.2 The Utsira formation

The Utsira formation is a long, narrow sandstone formation spanning a large portion of the central North Sea (Chadwick et al., 2004; Zweigel et al., 2004). Near the injection site the aquifer extends from a depth of about 1100m below sea level (bsl) to about 800mbsl, where it is capped by a 200–300m thick shale caprock. It consists of fine to medium grained, moderately well sorted sand, cut by intra-reservoir shale layers with an average thickness of

about 1 m and vertical separation of 30m (Zweigel et al., 2004). Porosity of the sand was determined to range from 35 to 40% (Holloway et al., 2000; Zweigel et al., 2004), and the sand is almost completely unconsolidated. The Utsira sand is about 300m thick in the Sleipner area, but the shale layers segment the sand into 30m sections, on average. The direct overburden consists of clay rich sediments with a thickness of about 250 m. The injection point is at a depth of 1012mbsl and the water depth is about 80 m.

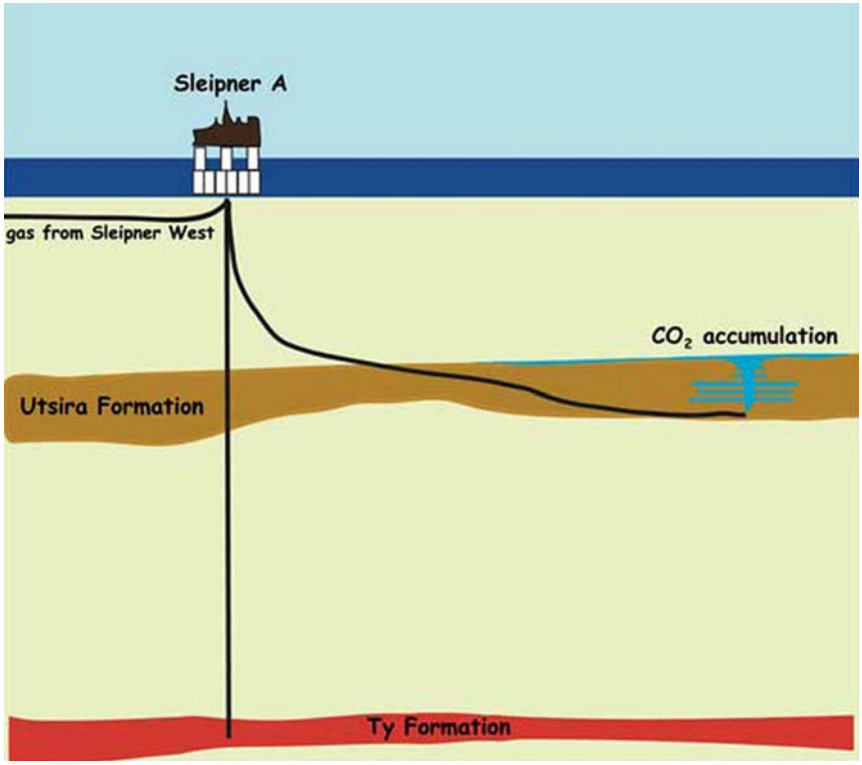

Figure 5-2: Cartoon illustrating the CO_2 injection operation at Sleipner. CO_2 is separated from the incoming gas, then injected into the Utsira formation.

5.2.3 Time-lapse reflection seismic surveys

In addition to a pre-injection 3D seismic survey in 1994, 3D seismic data were collected in 1999, 2001, 2002 and 2004. The seismic monitoring surveys all clearly show a signal from the injected CO_2 (Figure 5-3). By 1999, the CO_2 had reached the top of the Utsira sand and has since been spreading laterally as more of the CO_2 has migrated upwards. High amplitude subhorizontal reflections are caused by accumulation of CO_2 under the thin inter-reservoir shale layers (Arts et al., 2003; Chadwick et al., 2004), which act as temporary barriers to buoyantly driven CO_2 flow. The decrease in P-wave velocity due to the presence of CO_2 causes seismic pushdown, as events beneath the CO_2 layers are delayed in travel time. Pushdown can be seen on the seismic data in Figure 5-3 as an apparent downward dip in the reflective layers, increasing towards the center. The area-integrated pushdown (Chadwick et al., 2005), which depends on both the amount of CO_2 and the CO_2 saturation, has increased proportionally to the amount of injected CO_2.

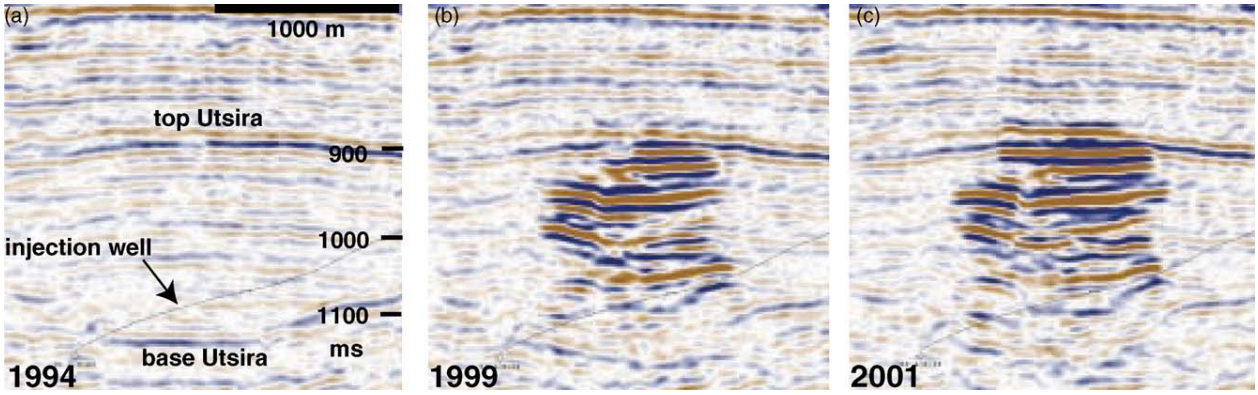

Figure 5-3: This figure shows the time-evolution of an east–west slice through the 3D seismic reflection data. (a) Seismic profile before CO_2 injection, (b) after 3 years of injection, and (c) after 5 years of injection. Data for this figure were provided by the SACS Consortium.

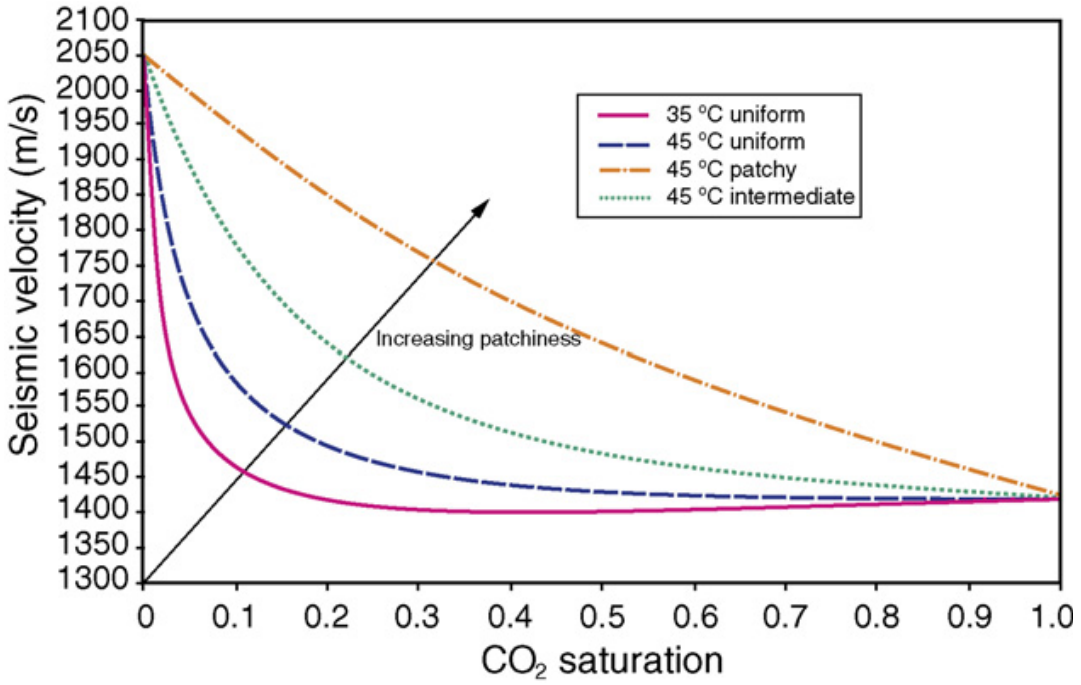

Figure 5-4: Velocity vs. CO_2 saturation curves derived from Gassman's relationships for the Utsira formation. The solid curve is for a uniform saturation with the reservoir temperature of 35 °C and ρ_{CO2} = 700 kg/m^3. The dashed curve is for a uniform saturation at 45 °C and ρ_{CO2} = 550 kg/m^3. The dash-dot curve is for a patchy saturation at 45 °C and ρ_{CO2} = 550 kg/m^3 and the dotted curve is for the same reservoir temperature but with an intermediately patchy distribution of CO_2. The two temperatures represent the expected end member scenarios for the reservoir.

Chadwick et al. (2000) modeled seismic velocity as a function of CO_2 saturation using Gassmann's relationships (e.g. Han and Batzle, 2004; Mavko and Mukerji, 1998; Nolen-Hoeksema, 2000; Wang et al., 1998). Figure 5-4 shows the P-wave velocity versus CO_2 saturation for the Utsira sand as predicted by Gassmann's relationships for different values of reservoir temperature (compare the uniform saturation curves). Because the rock matrix in the Utsira sand is weak, the compressional velocity is sensitive to the compressibility of the fluid,

which varies with temperature. The CO_2 density is assumed to be either 550 or 700 kg/m^3 in Figure 5-4.

By assuming the density of CO_2 within the reservoir is 700 kg/m^3 Chadwick et al. (2005) used seismic reflection amplitudes and pushdown to estimate an in situ mass of 2.01 MT compared to the known injected mass of 2.35 MT for 1999. In their model, the CO_2 within the reservoir was partitioned between high saturation thin layers and a low saturation volume existing in a diffuse form between the layers. The diffuse CO_2 is presumably a consequence of CO_2 percolating upwards from the layers through the overlying shales. However, reservoir flow simulation models indicate that extensive clouds of diffuse CO_2 are difficult to produce physically. The diffuse mass was assumed to have a vertically uniform distribution, yielding a minimum value for the CO_2 mass required to fit the data, since non-uniform or 'patchy' CO_2 distributions require more mass for a given seismic pushdown (Mavko and Mukerji, 1998). However, this makes it impossible to determine the mass of contained CO_2 without first determining the CO_2 saturation and density. In fact, two of the three quantities must be known in order to determine the third. Examples of two velocity versus average CO_2 saturation curves for patchy saturation models are shown in Figure 5-4. Furthermore, dissolution of up to 15 and 20% of the CO_2 into the formation water is a fundamental process of the injection (Johnson and Nitao, 2003) which decreases the observed mass. Also, incomplete ability to resolve the pushdown associated with the main chimney can cause the mass estimation to be low.

5.2.4 Utsira temperature and CO_2 density

One of the largest sources of uncertainty in seismic estimates of CO_2 mass comes from uncertainty in the density of CO_2 within the Utsira formation. The density of the injected mixture depends on the amount of trace impurities, temperature, and pressure. The carbon dioxide injected at Sleipner contains nitrogen (0.063%), ethane (0.123%), methane (0.9%), which tend to lower the density, and BTX (butanes, toluenes, and xylenes, 0.667%), which tend to increase the density. For this study, the impact of these impurities are neglected, meaning the thermodynamics and equation of state (EOS) for pure CO_2 are used (e.g. Span and Wagner, 1996).

The temperature profile through the formation is based on a single downhole measurement of 37 °C at a depth of 1058m bsl (Lindeberg et al., 2000; Zweigel et al., 2004), made at the time of drilling. For a water depth of 80m and assuming 4.8 °C on the seafloor, this gives a linear temperature gradient of 33 °C/km. However, this single measurement is subject to an uncertainty of up to 10 °C (Hermanrud, 1988; Rider, 1986; Williamson et al., 2001), because the measurement was made before the fluids in the borehole reached equilibrium, something that can take several months.

The problem is minimized when continuous temperature monitoring during drill stem tests is done. At the Sleipner natural gas field a total of 21 different drill stem tests measured a reservoir temperature of 101.7 °C with a standard deviation of 0.5 °C at 2600 m bsl (Hermanrud, 1988). This temperature was used as a basis for thermal modeling of the temperatures in the overburden rocks at Sleipner, including the Utsira formation.

The thermal modeling was done using BasinMod 1D (March 2005 release). Model parameters consisted of a thermal conductivity of 1.2 W/mK for shales and claystones, a thermal

conductivity of 2.4 W/mK for sandstones, and a seabed temperature of 5 °C. The heat flow was calibrated to match the observed temperature of 101.7 °C at 2600 m bsl. A porosity of 0.37 was used for the sandstone within the Utsira formation. The modeling predicts a temperature of 36.2 °C at the top of the Utsira formation (810mbsl), with a thermal gradient of 26 °C/ km within the Utsira. The average thermal gradient in the overburden section has is 38 °C/km. Sensitivity checks were performed by increasing the sandstone matrix thermal conductivity to 4 W/mK and by increasing the claystone thermal conductivity to 2W/mK. In both cases, the temperature at the base of the Utsira formation changed by 1.5 °C or less.

Further uncertainty in the calculations is related to how seabed temperature fluctuations during the last million years have influenced temperature in the underlying sediments. According to Mjøen (1988), seabed temperature fluctuations of 7 °C in the Pliocene/Pleistocene have resulted in corresponding temperature fluctuations of 2 °C at 1 km burial depth. By assuming a temperature ranged from 0 °C at the base of the ice sheets to 7 °C, the average seafloor temperature is approximately 4 °C. As the present day temperature of the seafloor is 3 °C above this average, the temperature of the Utsira formation is expected to be 1 °C higher than the average Pliocene/Pleistocene value. Therefore a seafloor temperature of 5 °C was used in the simulations. These arguments and modeling results suggest that the virgin rock temperature of the Utsira formation at 1058 m bsl is 42.5 °C, with an uncertainty (standard deviation) of 1 °C.

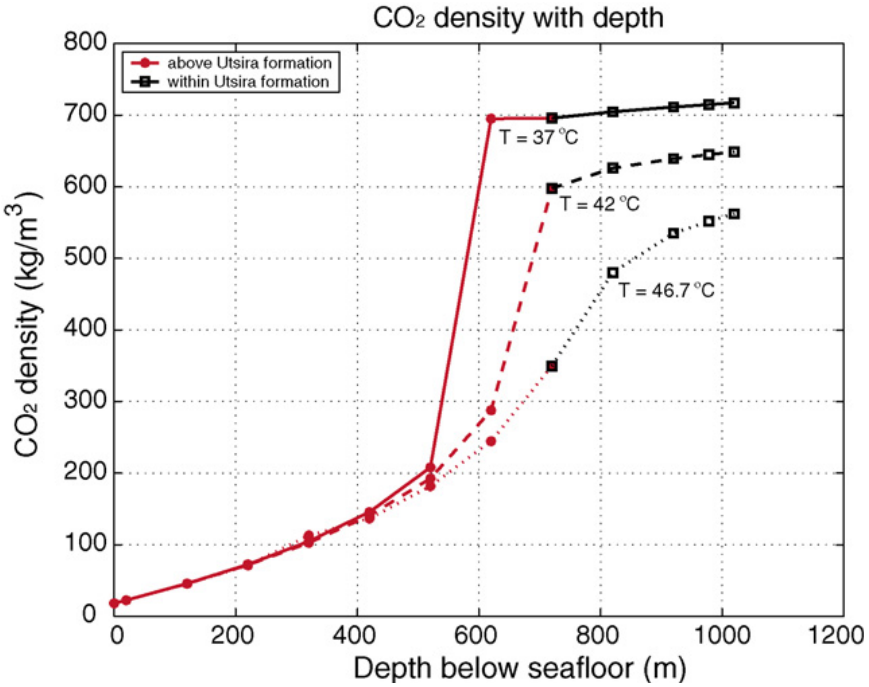

Figure 5-5: CO_2 density vs. depth for three possible temperature profiles in the Utsira formation. Because CO_2 goes through a critical phase transition, the resulting density is highly dependent on temperature. Thus a change in temperature of 5–10 °C can change the density estimate of the CO_2 by a factor of two.

However, near the predicted reservoir temperature and pressure conditions, CO_2 goes through a critical phase transition in which the density changes from 200 to over 700 kg/m^3 (Span and Wagner, 1996) (Figure 5-5). Thus a slightly higher temperature could result in a much lower CO_2 density. Additionally, the CO_2 will be heated during compression from the wellhead

conditions (25 °C, 64 bar) and down through the injection well. Because of the high injection rates, the injected CO_2 may experience close to adiabatic conditions, putting the temperature at a maximum of 57 °C at the bottom of the injection well. This could create an ultra-low-density front or plume of CO_2 surrounded by cooler CO_2. Until recently, most of the work that has been done in reservoir simulations and in estimating the in situ CO_2 mass has assumed that the 37 °C measurement is correct, and that the CO_2 density is 650–700 kg/ m^3. Therefore, determining the in situ CO_2 density is important for long-term modeling and predictions.

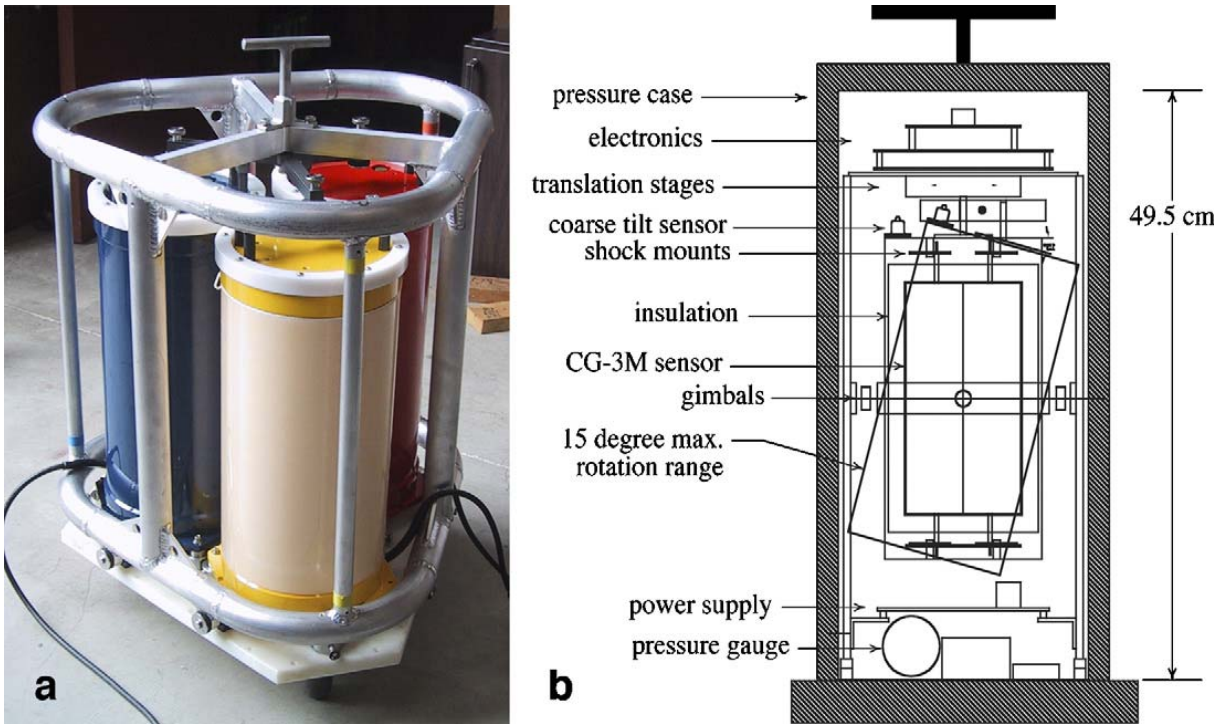

Figure 5-6: (a) Photograph of the ROVDOG instrument package used in the Sleipner gravity survey in 2002. Three instruments are affixed to one frame to increase the number of measurements at each site. (b) Diagram from Sasagawa et al. (2003) illustrating the internal schematics of the ROVDOG.

As CO_2 is injected into the Utsira sand, it displaces the water from the pore space in the sand, causing an effective bulk density decrease within the formation. One reservoir monitoring technique sensitive to changes in density is time-lapse gravity. Seafloor gravity measurements made with an ROV carried instrument have been shown to be capable of measurement accuracies of 18 μGal or less (Nooner et al., 2003, 2004; Sasagawa et al., 2003), comparable to land surveys. This instrument, the ROVDOG (Remotely Operated Vehicle deployable Deep Ocean Gravimeter), is well suited for this type of study (see Figure 5-6).

5.3 Gravity and pressure data acquisition

The procedure for the two surveys followed the method of Eiken et al. (2003). First, the vessel transited to a benchmark location, then the ROV was launched with ROVDOG held in place by the manipulator arm and a mounting bracket (e.g. Figure 5-7). The pilot guided the ROV to the benchmark, locating it acoustically and visually with cameras. Short baseline acoustic navigation of the ROV usually enabled benchmark location to within a few meters of

its expected location. Upon benchmark location, the pilot maneuvered the ROV into position, placed the ROVDOG on top of the benchmark and released it from the manipulator. The ROVDOG operators then initiated an automatic leveling routine and began the gravity and pressure measurement. During the measurement, the ROV thrust downward to hold its position on the bottom 1–2 m from the benchmark. The only link between the ROV and the sensors during the measurement was a cable, which was weighted to lay on the seafloor, thereby mechanically decoupling the sensors from the ROV. Each observation lasted for about 20 min. At the end of the measurement, data logging was terminated and the ROV pilot retrieved the ROVDOG with the manipulator arm. The ROV then began an under-water transit to the next site (followed by the vessel) at a typical speed of 1–2.4 knots. When the observation sites are separated by less than 1.3 km (as they are in the Sleipner array), this mode of transiting between benchmarks is more time efficient than recovering the ROV to the vessel. It affords the added benefit that the gravimeters remain at seafloor temperature, enhancing the survey repeatability.

Figure 5-7: HIROV 3000 Mk II ROV deploying the ROVDOG meters in 2002.

Concrete seafloor benchmarks were used because they are meant to serve as stable platforms to place the instruments in exact registration on the seafloor. These benchmarks are 35 cm tall and are frustum in shape, with a lower diameter of 160 cm and an upper diameter of 80 cm (Figure 5-8). This shape minimizes disturbance from trawl fishing. Each benchmark has a mass of about 650 kg. They have proven to be quite stable in a similar experiment in 300 m water depth (Stenvold et al., 2006), with a vertical stability of <1 cm over several years.

Twenty of the benchmarks were placed in a 7.3 km long WNW–ESE profile across the injection point (Figure 5-9). The distance between stations increases from about 300m near the injection point up to 500m toward the ends. The end points are far from the injection point and are perpendicular to the maximum spreading direction observed from the 1999, 2001, and 2002 seismic surveys. This geometry was chosen to maximize the lateral gravity gradient and minimize the change in gravity over time on the endpoints, which are designed to serve as temporally stable references in our relative surveys. Another 10 locations span the orthogonal dimension and cover the extent of the CO_2 accumulation in 2002. The benchmarks were

lowered to the seafloor with a wire line and acoustic release hooked onto a small chain, which fell into the central hole after release. The deployment operation lasted 10 h for all 30 benchmarks, and was done just before surveying, on 16 August 2002.

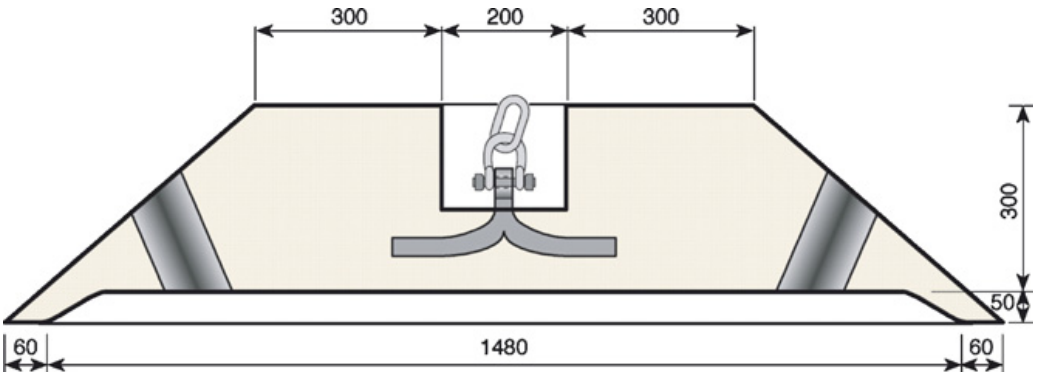

Figure 5-8: Vertical cross-section of the concrete frustum shaped benchmarks used at Sleipner to provide platforms for time-lapse gravity measurements. Dimensions are given in millimeters.

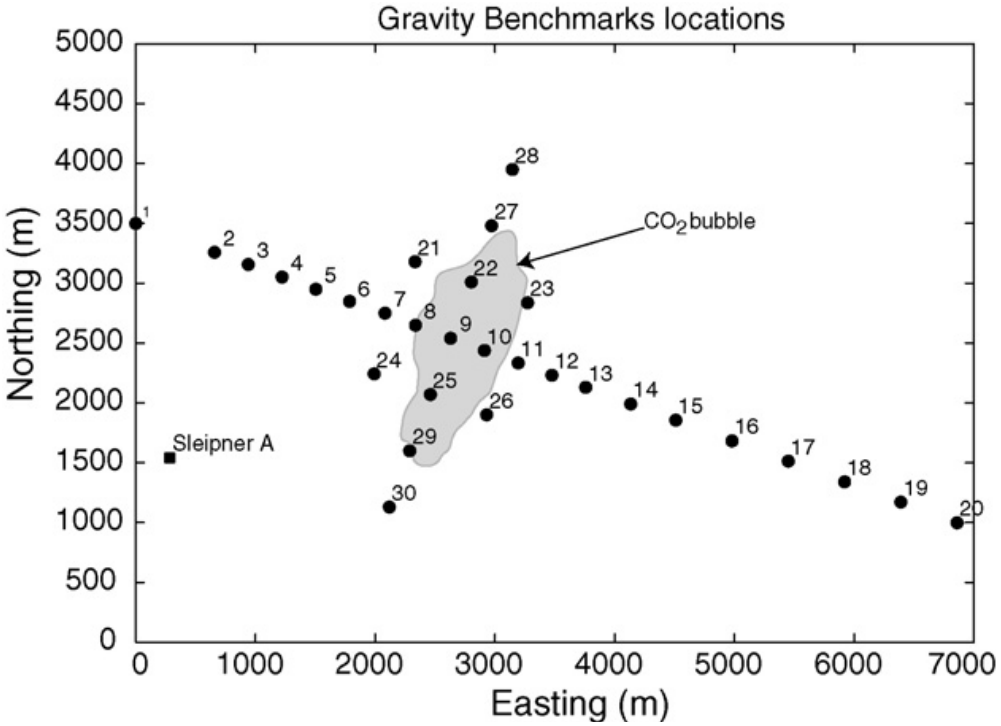

Figure 5-9: Map showing the benchmark locations in relation to the injected CO2 bubble. The outline of the CO2 comes from 2001 seismically imaged horizons.

5.3.1 2002 survey

Gravity measurements were carried out 16–20 August 2002 using the ship Edda Freya. One hundred and fifteen measurements were made during this time, at a rate of about 30 per day. Each station was visited at least three times, to give adequate control on drift and survey accuracy. Survey loops were made with benchmark SP09 as the central location (Figure 5-9). This site was visited 15 times for a loop duration of about 7 h. The sequence of stations within each loop was alternated in order to separate temporally correlated errors from spatially

correlated errors. The six stations with largest scatter (based on onboard processing) received a fourth visit, and the easternmost station (SP20), which is likely to be well outside the area of CO_2 influence and hence serve as a reference location for future gravity changes, received five visits. Table 5-1 shows the number of visits per station. ROVDOG Units 1, 2, and 3 were used throughout the survey. Power failure on Unit 3 caused a halt in the operation for repair after 31 measurements had been made. The instrument was brought on deck, the pressure case opened, a loose connector was repaired and it was put in the water again within 2 h. Weather was good during benchmark deployment and at the beginning of the survey but increasingly worsened. This can be observed in the noise level (RMS sample scatter) of the gravity time series (Figure 5-10). Significant wave heights were about 3 m towards the end of the survey.

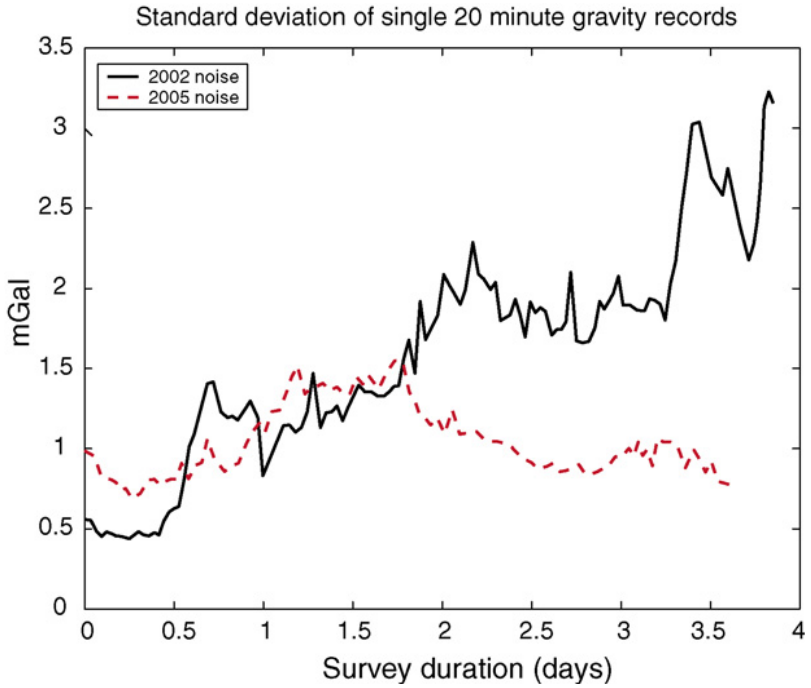

Figure 5-10: As the survey progressed, wind and wave height increased. This is reflected in the RMS scatter of 20 min gravity records, which is shown above for both surveys.

To aid with tide corrections, pressure was continuously recorded over the duration of the survey using portable seafloor instruments (made by Aanderaa Instruments) located at the center of the survey area (at benchmark SP09). Altogether, four reference gauges were deployed strapped together in pairs, two model WLR7 (Water Level Recorder) and two WLR8s. The two WLR7 pressure gauges show good agreement, but the WLR8 gauges deviated by about 20% from each other. Therefore, the data from the WLR8 gauges were discarded. The WLR7 gauges are rated to a depth of 340m and the WLR8 gauges are rated to 1370 m. The two WLR7 gauges agree to within 36 Pa (standard deviation), corresponding to a depth uncertainty of 3.6 mm. A CTD (Conductivity Temperature Depth) profiler attached to the ROV measured density profiles through the water column at every launch and recovery, for a total of four measurements, all at benchmark SP09.

5.3.2 2005 survey

The 2005 survey was done on board the supply vessel Normand Mjolne. The gravity survey was carried out 2–6 September 2005. The numbers of measurements at each benchmark are given in Table 5-1. The reference benchmark, SP20, was measured 5 times, and the central benchmark, SP09, was measured 12 times. A total of seven recoveries of the instruments to the ship were done, for long transits. ROVDOG Units 3, 4, and 6 were used throughout the survey. Units 4 and 6 are new models based on the sensor core of the Sintrex CG5 land gravimeter; Unit 3 is the same as in the 2002 survey and is based on the sensor core of a CG3-M land gravimeter.

Station	Latitude	Longitude	Number of visits		Gravity relative to SP20 (mGal)		Pressure relative to SP20 (kPa)	
			2002	2005	2002	2005	2002	2005
SP01	58.3842	1.9012	4	2	4.7644	4.7070	41.5851	43.0740
SP02	58.3821	1.9125	3	2	4.4375	4.4136	33.6682	33.7076
SP03	58.3812	1.9173	3	2	4.3141	4.2764	31.0152	32.3748
SP04	58.3803	1.9222	4	3	4.1420	4.1217	27.9551	27.8403
SP05	58.3794	1.9269	3	4	4.0087	3.9935	25.5377	25.2382
SP06	58.3786	1.9319	3	3	3.8820	3.8750	22.9969	22.7521
SP07	58.3780	1.9351	3	3	3.8002	3.7895	22.1030	22.0779
SP08	58.3768	1.9413	3	3	3.5279	3.5327	19.5980	19.3918
SP09	58.3759	1.9464	15	12	3.3174	3.3046	17.7361	18.4856
SP10	58.3750	1.9513	3	3	3.1505	3.1432	15.7740	16.0283
SP11	58.3742	1.956	3	3	2.8254	2.8250	13.7904	13.8325
SP12	58.3732	1.9609	3	3	2.6297	2.6274	12.1591	12.4415
SP13	58.3724	1.9657	3	3	2.4402	2.4255	10.4819	11.1114
SP14	58.3712	1.9722	3	3	2.0403	2.0352	9.2097	9.6559
SP15	58.3700	1.9787	3	2	1.7160	1.7237	7.6249	7.2191
SP16	58.3686	1.9868	4	3	1.2853	1.2779	5.1286	5.8440
SP17	58.3671	1.9948	3	3	0.9477	0.9323	3.2265	4.2854
SP18	58.3656	2.0029	3	3	0.4858	0.4879	1.8225	1.8706
SP19	58.3641	2.011	3	3	0.0589	0.0404	0.5356	1.4732
SP20	58.3627	2.0191	5	5	0.0000	0.0000	0.0000	0.0000
SP21	58.3817	1.9411	3	3	4.1823	4.1891	20.7117	20.3627
SP22	58.3802	1.9492	3	3	3.9437	3.9409	17.5053	17.6863
SP23	58.3787	1.9573	3	3	3.5904	3.6040	14.1962	13.8816
SP24	58.3732	1.9355	3	3	2.9725	2.9541	20.6325	21.1945
SP25	58.3717	1.9436	3	3	2.5839	2.5770	17.5178	18.1675
SP26	58.3702	1.9516	3	3	2.2108	2.2135	14.4556	14.4788
SP27	58.3844	1.952	4	3	4.4022	4.4398	16.8407	14.4265
SP28	58.3887	1.9548	4	2	4.9743	4.9689	17.0307	17.5382
SP29	58.3674	1.9408	3	3	2.0809	2.0906	16.8690	16.2933
SP30	58.3632	1.9379	4	2	1.5375	1.5399	15.6765	15.5697

Table 5-1: Details about each station for each year.

The sea state varied from 1 to 4 m maximum wave height, resulting in 1 s sample scatters ranging from 0.6 to 1.8 mGal (Figure 5-10). Since most of this noise is periodic, the contribution to the standard errors for a 20min average reduce to 0.001, 0.005, and 0.009 mGal for single a measurement for Units 3, 4, and 6, respectively. However, instrument drift,

changes in the local water density and temperature, tides, benchmark tilt, mechanical disturbance of the gravimeter springs, and other effects reduce this precision.

Five reference tide gauges were deployed, with two at benchmark SP20 and three at benchmark SP09. At benchmark SP20, one gauge was a WLR7 and the other was a WLR8. At benchmark SP09, there were two WLR7s and one WLR8. The data from the WLR8s did not agree well (σ = 0.17 kPa), so only the WLR7 data was used. Disagreement between the WLR7 gauges was 0.04 kPa (4~mm in depth), similar to the 2002 survey. A total of 11 CTD measurements were made throughout the survey. The mean value of these was used to determine the average water density at the survey depth.

5.4 Data processing

Much of the gravity and pressure data analysis was done onboard the ship during the survey for quality control purposes. After a measurement was completed on a benchmark, the raw data were processed immediately to examine data quality. After verifying the data quality, transit to the next site began. The resulting processed data were then put into a spreadsheet where drift and tide corrections were made. Instrument drift was computed based on repeat site measurements.

The steps of processing gravity recordings are as follows: (1) make tilt and temperature corrections to the data, (2) correct the data for solid earth and ocean tides, (3) edit out bad segments of data, (4) estimate instrument drift using a matrix inversion of all repeated sites, then subtract this drift, (5) take the mean of all three gravimeters with appropriate weights for each measurement, and finally (6) calculate the mean value of gravity at each benchmark from all repeats. Individual measurements were evaluated for consistency by examining differences among the meters and recovery effects (viscoelastic relaxation of the quartz spring) for each measurement. Large recoveries prompted the use of the second half of a record, rather than the entire record. A similar processing scheme was used for the pressure analysis: (1) subtract the reference pressure (tide signal) from the raw pressure, (2) estimate and subtract gauge drift, (3) calculate the mean of the three gauges for each site, (4) convert pressure to depth, and finally (5) find the mean depth for each benchmark. Once again, data quality was checked by comparing the differences among gauges for each measurement. Extreme outliers (>5σ) were not included in further analysis.

5.4.1 Pressure

The reference pressure gauges that were deployed during the survey provide a direct measurement of effects of the ocean tide, changes in air pressure, changing wind conditions, and any other time-varying environmental pressure signal that might contaminate the ROVDOG data. This reference data was subtracted from the 20 min ROVDOG pressure time series. The averages of each 20-min time series were then computed and compared for the three units. Gauge drift during the survey was calculated by fitting a straight line to all repeat measurements. Pressure was then converted to depth using a model with a constant water density of 1028 kg/m^3 (the approximate water density over the range of the survey—determined from the CTD measurements), gravity of 9.82 m/s^2, and air pressure of 101 kPa. The resulting water depths vary from 79.5 to 83.6 m. More details on the processing of the pressure data can be found in Stenvold et al. (2006).

For monitoring relative changes, depths are referenced to locations outside the area of gas injection, such as station SP20. The repeatability of the measurements gives the best indication of the uncertainty in the relative depth values. Figure 5-11b shows the residuals after the mean value of a station is subtracted from each measurement at that station. The standard deviation for the 2002 survey is 0.37 cm, which we adopt as the uncertainty in the relative depth estimates. Apart from three outliers, all values repeat to within ±0.8 cm. The depth values for 2005 have an uncertainty of 0.54 cm. The small depth range of 4.1m contributes significantly to the repeatability, as gauge precision scales with the range of operation, in part due to hysteresis effects.

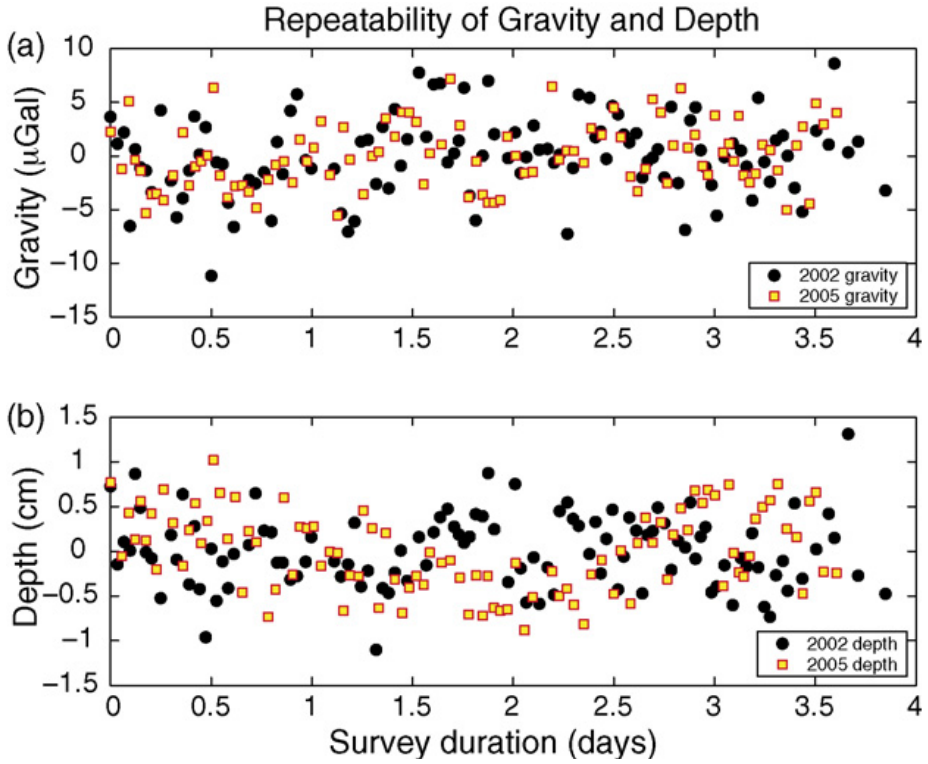

Figure 5-11: (a) Plot showing the scatter of repeated gravity measurements after the mean of each station has been subtracted from each measurement. Each point is the average of the three gravimeters. The standard deviation of the results (4.3 μGal for 2002 and 3.5 μGal for 2005) indicates the precision of the gravity values for the stations. (b) Plot showing the scatter of repeat pressure measurements after the mean for each station has been subtracted. Each point is the average of the three pressure gauges. The standard deviation of the data points is 0.37 cm for 2002 and 0.54 cm for 2005.

5.4.2 Gravity

For each 20 min long gravity record, noisy samples were eliminated and the time range of good data selected, prior to calculating the average. Narrow-band seafloor accelerations (mostly at 2–3 s period) originate as an interference phenomenon between ocean waves from different directions (Babcock et al., 1994; Longuet-Higgins, 1950). Noise amplitudes in this band were up to 3.5 mGal near the end of the survey, but due to the periodic nature a 20min average effectively reduced the noise to acceptable levels.

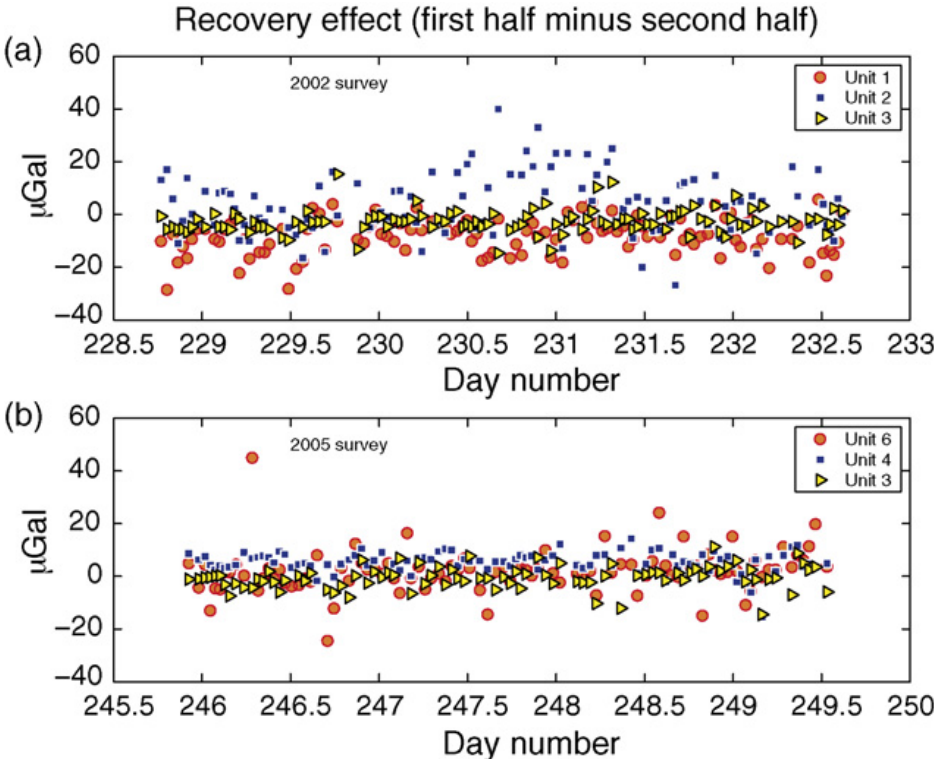

Figure 5-12: Plot showing the recovery effect for each of the three ROVDOG gravimeters. The plot shows the mean of the first half minus the mean of the second half of each 20 min gravity record for (a) 2002 and (b) 2005.

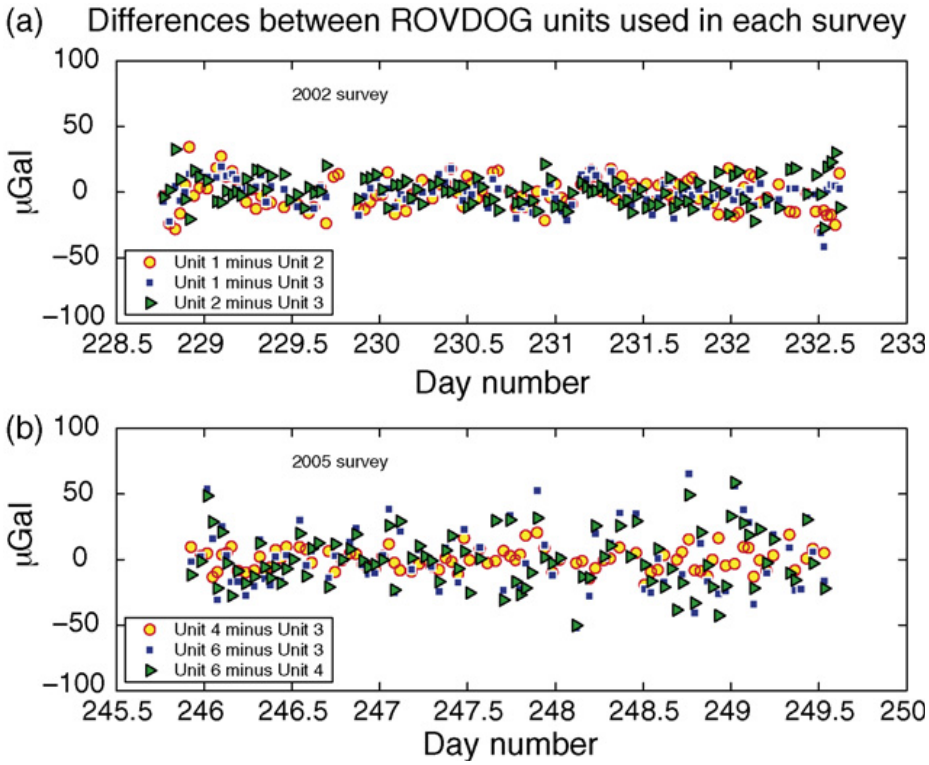

Figure 5-13: Plot showing the differences among the three ROVDOG gravimeters at each site for (a) 2002 and (b) 2005. No apparent trend shows up in the plot, indicating that the drift correction is good.

The quality of the relative gravity data is evident in the repeatability of the measurements. Quality control was done by comparing repeated observations in three ways: (1) stability of each measurement was examined by comparing the first and second half of each 20min gravity record. (2) Agreement among the 3 meters was examined for each measurement. (3) Multiple measurements made at each benchmark were compared.

During transit from site to site, the ROVDOG package is subject to ROV motions and vibrations. When a gravity meter is tilted, its quartz spring becomes shorter. During the time the spring has been shortened, visco-elastic deformation of the spring takes place and some time is required for the spring to ‘‘recover’’ from this altered state when making the next measurement. This behavior, called the recovery, can last up to 10 min based on laboratory experiments. The size of this effect is indicated by comparing the mean of the first half and second half of a 20min record (Figure 5-12). The recovery phenomenon is smallest on Units 3 and 4, and largest on Units 1 and 2. Due to the recovery, the first half of a gravity record was frequently discarded.

Gravity values were corrected for solid earth tides and the ocean loading term by using the worldwide model SPOTL (Agnew, 1996). The varying gravity attraction from water tide was compensated using sea level height estimates based on the reference pressure measurements and the average water density determined from CTD measurements.

Instrument drift was estimated individually for each gravity meter by least squares fitting all repeat measurements to a third order polynomial in time. In 2002, a change in drift rate occurred for Units 2 and 3 at the time when Unit 3 was recovered to the surface to replace a faulty connector (decimal day 229.7). Therefore, separate drift polynomials are used before and after the incident (Table 5-2) for Units 2 and 3. This could be due to temperature fluctuations, as laboratory tests have indicated that instrument drift is sensitive to changes in external temperature.

		Linear term (μGal/day)		Second order term (μGal/day^2)		Third order term (μGal/day^3)	Split time (day)
		First half	Second half	First half	Second half		
2002							
	Unit 1	556.5		-1.7		NA	NA
	Unit 2	362.8	442.4	0	-0.1	NA	229.7
	Unit 3	177.9	192.7	-30.6	0.6	NA	229.8
2005							
	Unit 3	417.5		5.9		-2.5	NA
	Unit 4	181		0.3		-2.7	NA
	Unit 6	328.4		1.9		-5.1	NA

Table 5-2: Gravimeter drift rates for Units 2 and 3 changed mid-survey in 2002 when the instruments were recovered to the surface to replace a faulty connector (at decimal day 229.7).

The drift correction can be quality controlled by plotting unit differences as a function of survey time (Figure 5-13). There are no apparent trends left in the plot, which suggests the drift has been removed (drift values are given in Table 5-2). Unit differences also provide a check if one of the gravimeters is behaving differently or erratically. For example, Unit 6

appears to be behaving erratically for the last day of the 2005 survey. This can be seen as increased scatter in the U6–U3 and U6–U4 data sets.

In 2002, the repeatability (standard deviation of repeat measurements with averages removed) of the units were 8.8 μGal for Unit 1, 9.9 μGal for Unit 2, and 4.7 μGal for Unit 3. Because of the much better performance of Unit 3, it was heavily weighted in the average calculation. After weights of 0.2, 0.1, and 1 were given to Units 1, 2, and 3, respectively, the repeatability is 4.3 μGal (Figure 5-11a). The 2005 gravity values have a repeatability of 3.5 μGal (Figure 5-11a), after weights of 0.8, 1, and 0.1 were given to Units 3, 4, and 6, respectively.

5.5 Time-lapse results

Changes in gravity over time are found by subtracting the 2002 results from the 2005 results. After corrections for tide and drift were made, there remains a long-wavelength gravity trend increasing to the west. This trend has an apparent maximum value at benchmark SP01 (the western most station) of about 0.03–0.04 mGal. The most likely source of this signal is from water influx into the Ty formation, a natural gas reservoir that is being produced well below the Utsira formation and west of the injection point. Production from this reservoir is expected to cause an increase in local gravity due to a rise in the reservoir water as the natural gas is removed. Other possible sources for a long-wavelength gravity trend are massive sediment transport from the west to the east of the survey region or dispersed leakage of CO2 from the Utsira. Both of these possibilities seem improbable. A forward model was calculated based on the gas reservoir geometry, porosity, temperature, gas production data, and data from monitoring wells (all proprietary information of the Sleipner production license partners).

The time-lapse gravity and depth data are shown together in Figure 5-14a. The depth changes have a scatter of ~7 cm, with no apparent spatial correlation. This result is surprising since no subsidence was expected for the area, and we have not observed similar behavior at other sites in the North Sea (Stenvold et al., 2006). Changes in the gravity coincide nicely with the changes in depth, providing assurance that the observed depth changes are real. However, this means that the benchmarks are not as stable at Sleipner as at other North Sea sites in deeper water (Sasagawa et al., 2003; Stenvold et al., 2006). There are several pieces of information that can be used to limit the possible sources of benchmark motion which are explored below.

Trawl fishing in the area is not uncommon. Some benchmark disturbance by trawlers is evident from the fact that benchmark SP27 was not located in the position it was in 2002. Under each benchmark lived a family of steinbit (also wolf-fish or Atlantic catfish). These fish are large (up to 1.25 m) and feed on sea urchins, mussels, cockles, and crabs. Surrounding each benchmark was a few square meter area littered with shells discarded after feeding. Upon finding the benchmark coordinates, we found a mound of shells but no benchmark. Tracks from the dragged benchmark enabled us to locate it 20m to the northeast, with no shells in the vicinity, indicating that the benchmark had been moved recently. All other benchmarks were located in the expected place and no biological or morphological evidence suggested movement. Navigation was good to about 1m, however, so small movements cannot be precluded.

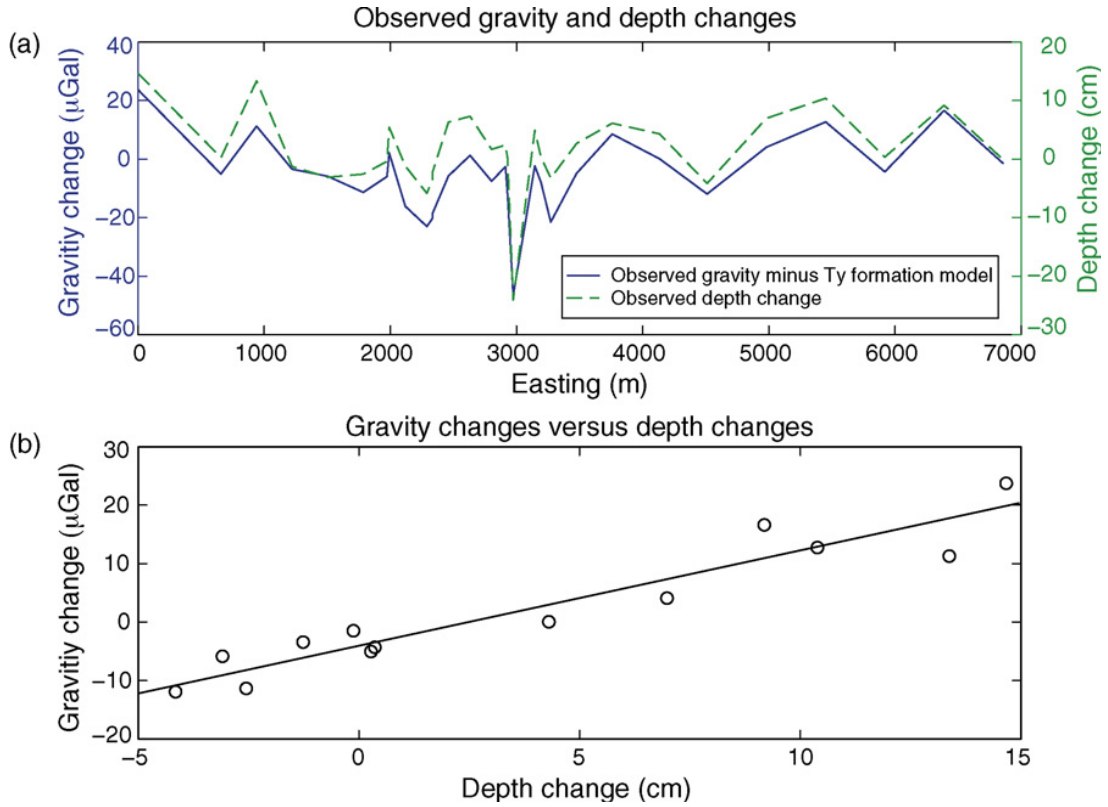

Figure 5-14: The correlation between depth changes and gravity changes is shown in two ways. (a) Variations in gravity (after subtracting a long-wavelength gravity trend due to gas production in the underlying Ty formation) correlate with changes in depth, and appear to be randomly distributed. The fact that the two are so similar provides evidence that the changes are real. (b) Gravity changes are plotted against depth changes for the outermost benchmarks. The slope of the best fitting line is the gravity gradient (0.16 mGal/m). See the text for details.

In addition to lateral movements, benchmarks could have been tilted by trawlers. Benchmark tilt was estimated using the coarse motor position voltages for the ROVDOG leveling gimbals. Doing this for both 2002 and 2005, it is evident that some of the benchmarks have become tilted since the first survey. Benchmarks SP01, SP09, SP13, and SP20 appear to be tilted 2–3° more than they were in 2002, while benchmarks SP10, SP18, and SP25 are tilted by 1–2° more. The remaining benchmarks are within a degree of the 2002 tilt values. Benchmark SP20 also had a mound of sediment (a few centimeter thick) on one edge, which could be evidence of some disturbance by trawl fishing. Additionally, in order for at least two large fish to live under each benchmark, there must be a large cavity (maybe 10 cm deep) underlying each benchmark. A 10 cm cavity under each benchmark would cause a decrease in observed gravity by 0.002 mGal, but would not affect the gravity gradient. However, a benchmark could sink and/or tilt due to such a large underlying cavity. Trawling could disturb a benchmark enough to shift it by a few centimeter over the underlying cavity, thereby causing it to sink and tilt. Corrections for benchmark tilts were made to the pressure gauges based on an empirical formula (Chadwick et al., 2006; Nooner, 2005). Without this correction, the maximum uncertainty introduced by a tilt of 28 is about 9 mm for depth and 2 μGal for gravity.

Although we did not look for evidence of scouring during the survey, sediment scouring is common in marine environments (e.g. Sumer and Fredsoe, 2002; Whitehouse, 1998), and has been observed extensively in the North Sea (e.g. Heerten, 1981). At 80m depth the orbital velocity of the water at the seafloor would be enough to move the sediment during storms of 10m significant wave heights (Soulsby, 1998). Tidal flows might also be enough to move sediments. Biological disturbances (such as from burrowing fish) can also increase the amount of scouring in some cases (Whitehouse, 1998).

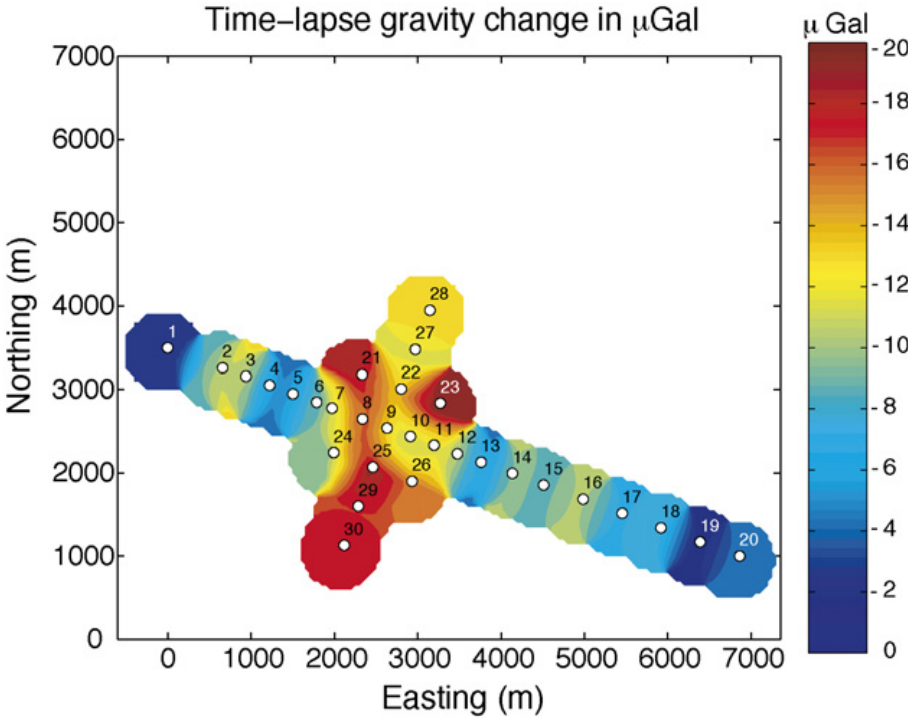

Figure 5-15: A smoothed version of the gravity residuals after correcting for depth and for the modeled gas/water contact rise in the Ty formation. Note the spatially coherent gravity decrease from 2000 to 4000m easting.

The time-lapse gravity data was inverted to simultaneously solve for a scale factor to the Ty formation forward model and the free water gravity gradient. Gravity data from only the outer benchmarks was used, to remove the influence of the injected CO_2 from the inversion. Figure 5-14b shows the best fitting line to the dg versus dz data after the Ty formation model has been subtracted. The best fitting value is $dg/dz = 0.16 \pm 0.04$ mGal/m, which is significantly lower than the theoretical value of 0.22 mGal/m.

A combination of factors may account for this. First, the gradient would be reduced by 0.027mGal/m due to the replacement of sediment with the concrete of the benchmark as the benchmark sinks into the sediments over time; however, not more than a few centimeters of benchmark settling was observed. Second, scouring of sediment surrounding each benchmark and concurrent benchmark subsidence (due to removal of underlying sediments) would cause an additional decrease in the observed gradient of 0.038 mGal/m. The resulting gradient would then be somewhere between 0.182 and 0.155 mGal/m, depending on the amount of benchmark settling. Thus the observed 0.16mGal/m is a reasonable value.

The horizontal gravity gradient in the area has not been observed to exceed 1.3 μGal/m, meaning that the benchmarks could have moved laterally 5m at most, assuming that the scatter in the depth gradient corrected gravity data comes from lateral motions. This is unlikely, given the position accuracy of the ROV. From the above arguments, it seems likely that the benchmark motions were primarily due to subsidence from scouring and settling, however, the benchmarks at Sleipner are not as stable as we had hoped.

Figure 5-15 shows the resulting depth and Ty formation corrected time-lapse gravity values. Each point has been smoothed by averaging all observations within a 500m radius of that point. For time-lapse changes, uncertainty is related to determining the reference zero-level, obtained by using stations outside the area of influence of the CO_2 injection. The uncertainty in time-lapse depth changes of each station is 0.9 cm, which maps into an uncertainty in gravity of 1.4 μGal. With its five visits in 2002, the southeastern most station (SP20) has an uncertainty in gravity of 1.9 μGal. SP20 also received five visits in 2005, for an uncertainty of 3.2 μGal. The total time-lapse uncertainty in the gravity measurements, accounting for uncertainty in the reference benchmark depth, is 5.3 μGal. A dip in the gravity with a maximum observed decrease of about 15 μGal can be seen in the data from an easting of ~2000 to 3000 m. This is the region of expected gravity decrease due to CO_2 injection. Benchmark SP03 (located at an easting of about 1000 m) also shows a dip in gravity. However, this is not spatially correlated with surrounding sites, suggesting that it is a spurious point. Benchmarks SP29 and SP30 are similarly low, suggesting spread of CO_2 to the south. This residual time-lapse gravity signal can be compared to forward models to help constrain the average CO_2 density, saturation, and flow geometry.

5.6 3D forward modeling

5.6.1 Modeling time-lapse gravity changes using seismically imaged CO_2

Expanding from Chadwick et al. (2005), any viable plume saturation model must satisfy the following conditions: (1) it must reproduce observed seismic reflectivity. (2) It must produce the observed seismic velocity pushdown. (3) The volume of CO_2 in the model must match the known injected volume. (4) It must produce the observed gravity change. (5) It must produce the observed seafloor deformation. Modeling of the expected seafloor deformation has shown that a maximum uplift of 0.01 mm/year is expected (Nooner, 2005), which is far below our capability to resolve.

The seismic data from 1999 to 2001 provide the most complete coverage of the CO_2 bubble, therefore the data from these years were used to build models of injected CO_2 for two scenarios. The first is for an average CO_2 density within the reservoir of 700 kg/m^3, and the second is for an average CO_2 density of 550 kg/m^3, corresponding to low reservoir temperature (35 °C) and high reservoir temperature (45 °C) scenarios, respectively. These models contain supercritical CO_2 in two distinct parts. The first is CO_2 residing in thin, high saturation layers, which have ponded beneath nine thin inter-reservoir shale layers (Figure 5-16a). These can be seen as layers of increased reflectivity in the time-lapse seismic data (Figure 5-3). The second volume of CO_2 is a low saturation diffuse volume occupying the space between the high saturation layers. This diffuse volume of CO_2 does not cause increased reflectivity, but its existence is indicated by a larger observed seismic pushdown than is expected from the high saturation layers alone. The amount of diffuse CO_2 is uncertain, and depends upon the CO_2 density and upon the details of its distribution. The

modeling approach is similar to Chadwick et al. (2005) with the following steps: (1) calculate a thin-layer model for the high saturation CO_2 layers. (2) Calculate the gravity from this model. (3) Calculate the velocity pushdown from this model. (4) Subtract the calculated pushdown fromthe observed pushdown to obtain the residual pushdown. (5) Use the residual pushdown to calculate the average vertical saturation for the diffuse volume. (6) Calculate the gravity from the diffuse CO_2 model and combine with the gravity calculated from the layers. (7) Compute the total mass and volume of CO_2 in the combined model.

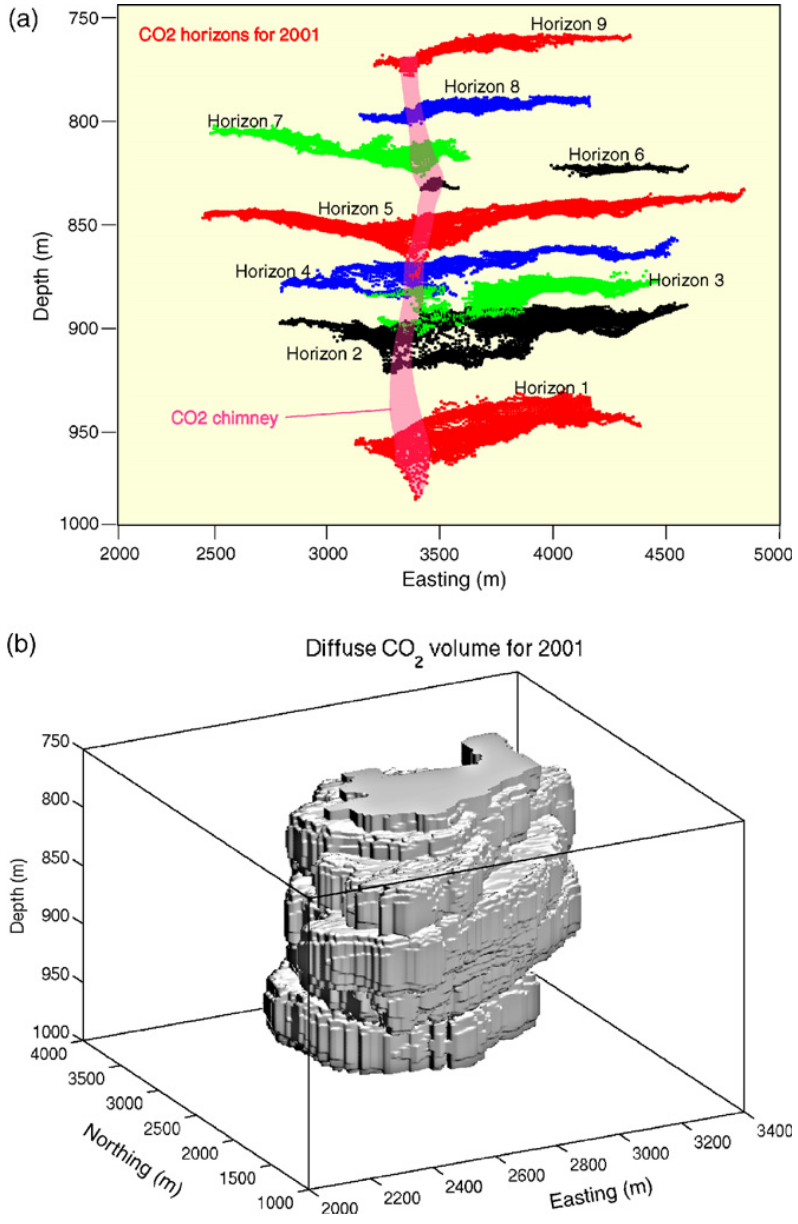

Figure 5-16: (a) A cutaway view of the seismic horizons used to construct the thin layer portion of the seismic models. (b) The volume enclosing the diffuse, low saturation CO_2 in the models based on the time-lapse 3D seismic data for 2001.

The reflection amplitude of the seismic horizons was provided as xyz data by the SACS (Saline Aquifer CO_2 Store) consortium. To work with the data, each horizon was first converted into a regularly spaced grid. The reflection amplitudes of the horizons were then

linearly related to layer thickness with the maximum reflection amplitude being set equal to 8m, corresponding to the tuning thickness of the seismic wavelet (Arts et al., 2002). The mass of CO_2 at each grid point is given by

$$m = \rho_{CO_2} S_{CO_2} \phi \, dxdydz \tag{5.1}$$

where dx and dy are the grid spacings, dz the layer thickness, ρ_{CO_2} the density of CO_2, ϕ the porosity, and S_{CO_2} is the saturation of CO_2. The only unknown is the saturation of CO_2, which varies with height, h, in each CO_2 layer due to capillary pressure, p_c, between the formation brine and injected CO_2. This relationship in SI units was determined by centrifuge experiments on core material from the Utsira Sand (Chadwick et al., 2004, 2005):

$$\Delta\rho g h = p_c = 810.35(1 - S_{CO_2})^{-0.948} \tag{5.2}$$

In the above equation p_c is the capillary pressure in Pa, $\Delta\rho$ the difference in density between water and carbon dioxide, and g is the gravity in m/s^2. The mass of CO_2 at each grid point can then be calculated from equation 5.1 using the layer thickness at each gridpoint and the average CO_2 saturation obtained from equation 5.2.

The thin layer mass for the low-density CO_2 case is 0.853 MT in 1999 (36.3% of the injected amount) and 1.5 MT in 2001 (34.0% of the injected amount). For the high-density CO_2 case, the mass is 1.53 MT in 1999 (65.1% of the injected amount) and 2.69 MT in 2001 (61.2% of the injected amount). Uncertainty in these figures comes from uncertainty in the interpretation of the seismic horizons, errors in the simple amplitude to thickness conversion, and reflectivity attenuation in the deeper parts of the plume which are difficult to quantify (Chadwick et al., 2005). An in house 3D gravity modeling code was then used to compute the gravity signal from the thin CO_2 layers. These results are shown in Table 5-3.

The seismic pushdown from the layers is the difference in two-way travel time (twtt) caused by the presence of the CO_2. This can be found from the change in seismic velocity, determined using Gassmann's relationships. The velocity changes rapidly for low saturations, but for saturations larger than about 0.2 it changes very little, particularly for homogeneous distributions. The pushdown for each density scenario for both years was then calculated and subtracted from the total observed pushdown to give the residual pushdown. This residual pushdown is caused by CO_2 that is not present in the thin layers, and requires the presence of additional CO_2 within the reservoir.

The next step, then, is to use the residual pushdown to estimate the saturation and mass of the diffuse CO_2 volume using the velocity versus saturation curves shown in Figure 5-4. The pushdown, ΔT, is defined as follows:

$$\Delta T = 2\left(\frac{1}{Vs_{CO_2}} - \frac{1}{V}\right)dz \tag{5.3}$$

where Vs_{CO_2} is the seismic velocity with CO_2 present, V the velocity without the presence of CO_2, and dz is the vertical thickness of the CO_2. To solve for Vs_{CO_2} from equation 5.3, an estimate must be made for the vertical thickness, dz. This introduces a non-unique element into the problem. An infinite number of distributions of diffuse CO_2 can be made to satisfy the residual pushdown. To estimate dz in a meaningful way, a volume enclosing the diffuse CO_2 was defined. A reasonable assumption is that the diffuse CO_2 resides near the higher saturation volumes (the thin layers and the chimney), but is not found some characteristic distance away, which was chosen to be 25 m. This value is two times the grid spacing and is

close to the average distance between shale layers, which is 30 m. Therefore, an algorithm stepped through the seismic horizons and every grid point within the characteristic distance from a high saturation grid point was included in the volume. Points that were within 1.75m of a seismic horizon (corresponding to the average CO_2 layer thickness) were excluded from the volume. This created the gridded 3D volume enclosing the horizons shown in Figure 5-16b. The vertical thickness, dz, was then calculated by summing the number of grid points in each vertical column included in the volume and multiplying each resulting number by the vertical grid spacing (12.5 m). The residual pushdown, ΔT, and the vertical thickness, dz, were then used together to solve for the average velocity, Vs_{CO_2}, through the diffuse CO_2.

	Year					
	1999	1999	1999	2001	2001	2001
CO_2 density (kg/m^3)	350	550	700	350	550	700
Total injected mass (MT)	2.35	2.35	2.35	4.26	4.26	4.26
Horizon mass (MT)	0.82	1.28	1.56	1.52	2.25	2.73
Horizon *g* (μGal)	13.4	8.9	5.9	21.8	14.6	9.7
Diffuse mass (MT)	0.1	0.15	0.38	0.18	0.28	0.75
Diffuse *g* (μGal)	1.7	1.2	1.6	2.9	2.1	3
Total *g* (μGal)	15.1	10.1	7.5	24.7	16.7	12.7
Total mass (MT)	0.97	1.43	1.94	1.7	2.53	3.49
% of total mass	41.12	60.94	82.75	39.88	59.36	81.85
Only the magnitude of the maximum changes are given						

Table 5-3: Summary of modeling results for seismic horizon models

A density of CO_2 was then chosen and Vs_{CO_2} was then used to determine an average CO_2 saturation value at each point using the appropriate velocity versus saturation curve from Figure 5-4. Because the seismic velocity changes very little for saturation values greater than 0.2, small errors in the calculation of Vs_{CO_2} can lead to large uncertainties in the resulting saturation estimate. These uncertainties are difficult to quantify. Nevertheless, the resulting model for the diffuse volume is a CO_2 distribution in which the CO_2 saturation varies laterally, but is constant vertically. This provides a good estimate of the gravity field, since the shape of the CO_2 bubble is a flat disc with a thickness to diameter ratio of 0.3 (meaning vertical variation in the CO_2 distributions does not affect the gravity much).

The mass in the diffuse volume can then be calculated from equation 5.1. For the low-density case, the diffuse CO_2 contains 0.15 MT for 1999 and 0.28 MT for 2001. Adding this to the thin layer mass gives 1.43 MT for 1999 (60.94% of the known injected mass) and 2.53 MT for 2001 (59.36% of the known injected mass). For the high-density case, the diffuse CO_2 contains 0.384 MT for 1999 and 0.752 MT for 2001. Adding this to the thin layer mass gives 1.94 MT for 1999 (82.75% of the known injected mass) and 3.49 MT for 2001 (81.85% of the known injected mass).

The contribution of the diffuse volume to the gravity signal is then calculated. Table 5-3 shows the contribution of each part of the model to the maximum gravity signal for each density scenario. Combining the layer contribution with the diffuse volume contribution indicates that the high-density scenario predicts a maximum change of about 2.7 μGal/year, while the low-density scenario predicts a maximum change of about 3.5 μGal/year (Figure 5-17).

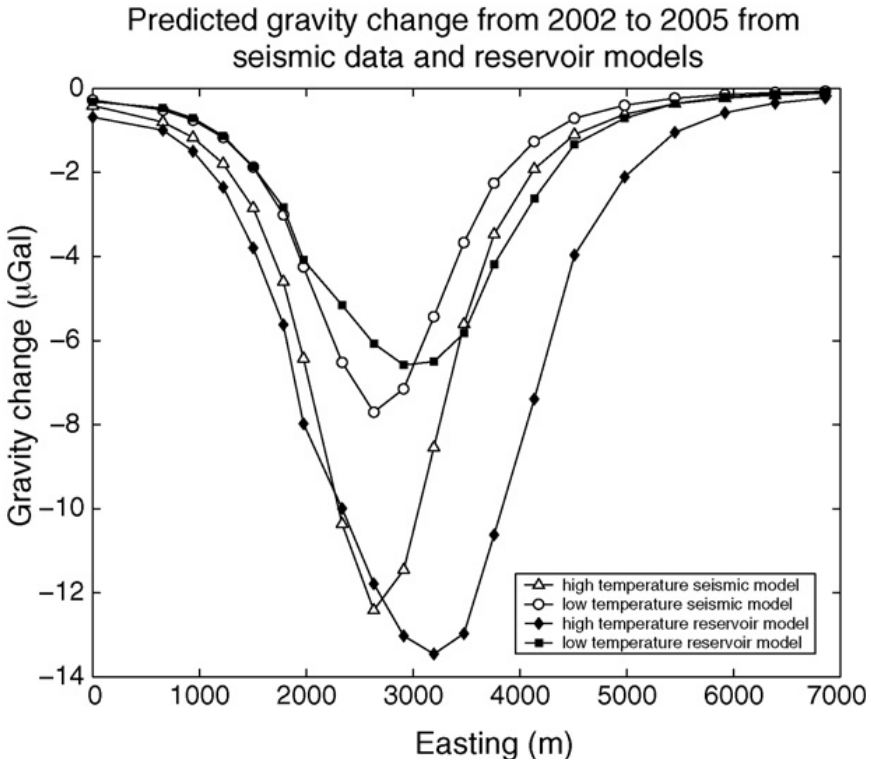

Figure 5-17: The predicted gravity change along the main NW– SE line, calculated from both the 1999 and 2001 seismic data and from the models IIa and IIb reservoir simulation models. The points along the line represent the seafloor benchmarks SP01–SP20 (Figure 5-9). Calculations were made using two different densities, 550 and 700 kg/m^3, corresponding to high and low reservoir temperatures, respectively.

5.6.2 Modeling time-lapse gravity changes using reservoir simulation models

Reservoir simulation models provide insight into the physical behavior of the injected CO_2 with things such as flow geometry, dissolution into the formation brine, and CO_2 saturation. These models, however, are highly dependent on reservoir characteristics such as temperature and CO_2 density. Therefore, calculating the expected gravity change on the seafloor from reservoir flow models provides a way, independent of seismic data, to use time-lapse gravity to put constraints on the density (hence average temperature) of CO_2 within the Utsira formation. Reservoir modeling at Sleipner has been done by SINTEF, an independent research organization. SINTEF produced 3D saturation grids from CO_2 flow simulations using the commercial reservoir modeling software Eclipse. The models were for a 3D volume with a permeability of 2 darcy and a porosity of 0.38, cut laterally by five impermeable layers (representing shale). The shape of these layers was guided by, but not matched to, the geometry of the seismically imaged CO_2 horizons. The boundaries of the model volume were kept at a constant pressure, simulating an infinite reservoir (Mo, S., personal communication, 2003). Two types of simulation models were examined. The first type, model I, has a central chimney and horizontal CO_2 layers like the seismic model; however, it has no low saturation volume (Figure 5-18a). The engineers at SINTEF have not been able to produce a CO2 flow scenario resulting in a low saturation volume as suggested by the seismic pushdown. Therefore, a second model was examined, model II, composed of several micro-chimneys, which, if small enough, might look like a diffuse volume of CO_2 to seismic energy (Figure

5-18b). This was created by randomly distributing 640 holes of increased permeability within the impermeable shale layers. Simulations for model II spanning 20 years were computed by SINTEF for average reservoir temperatures of both 37 and 45 °C, corresponding to CO_2 densities of ρ_{CO_2} = 750 kg/m^3 and ρ_{CO_2} = 550 kg/m^3 (call them models IIa and IIb, respectively). The reservoir simulations also predict the amount of CO_2 that dissolves in the brine over time. Therefore, the mass contributing to the gravity signal will be the total injected amount of CO_2 minus the dissolved CO_2.

The output of each flow model is a volumetric CO_2 saturation grid containing 428400 grid points (70 × 85 × 72). The thickness of the grid blocks varies from 15.2 to 0.2 m with depth, as the grid is refined below the shale layers (where most of the CO_2 resides). The horizontal grid spacing is constant at dx = 34.4m and dy = 36.1 m.

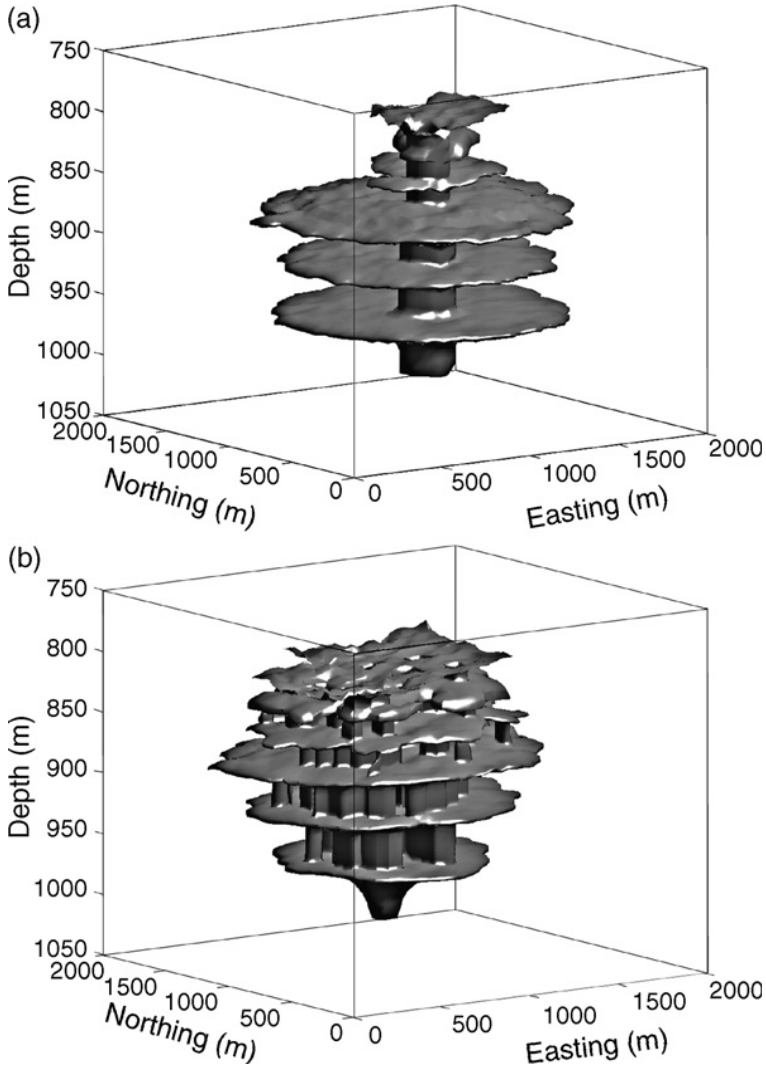

Figure 5-18: The reservoir simulation models. (a) The central chimney model, model I. (b) The random holes model, models IIa and IIb.

In the current study, saturation, S_{CO_2}, was converted to a change in mass at each grid point using a reservoir porosity of ϕ = 0.37, a shale fraction of v_{sh} = 0.01, a cell volume of V = dx × dy × dz, and a CO_2 density ρ_{CO_2} dependent on the flow model:

$$\Delta M = \Delta\rho V \phi (1 - v_{sh}) S_{CO_2}, \quad (5.4)$$

where $\Delta M = M_{CO_2} - M_{H_2O}$ and $\Delta\rho = \rho_{CO_2} - \rho_{H_2O}$. Gravity was then calculated from ΔM at each grid point.

The time-varying gravity spanning 1996–2002 computed on the seafloor benchmarks from model I indicates a maximum gravity change of about 2.2 μGal/year. Model IIa spans the years 1996–2016 and predicts a maximum change of about 2.4 μGal/year. Interestingly, the results are almost identical, in spite of the fact that the models have different dissolution rates for CO_2 into the aquifer brine. Model I is composed of a horizontal layers central chimney, while model IIa is composed of horizontal layers and multiple vertical chimneys. This means that model IIa has a larger surface area of CO_2 in contact with the brine, allowing more dissolution to take place (~4.5% in model I and ~17.5% in model IIa). Therefore, for the same amount of injected mass, model I has more undissolved CO_2.

Model IIb predicts a maximum gravity change of 4.7 μGal/year. The higher temperature of model IIb causes the CO_2 density to decrease, creating a larger density difference between the CO_2 and formation water. The lower density CO_2 also occupies more volume within the reservoir, increasing surface area in contact with the brine. The dissolution into water in this case is more than 23%. The lower density CO_2 is also more buoyant, which tends to increase the gravity driven vertical flow. Therefore, compared to model IIa, more mass in model IIb is located in the shallow layers.

5.7 Discussion

5.7.1 Density estimate

By modeling the seismically imaged horizons in 1999 and 2001 as thin, high saturation layers and the residual seismic velocity pushdown as a low saturation non-reflective diffuse volume of CO_2, estimates for in situ CO_2 mass can be made. However, not all of the known injected amount of CO_2 is accounted for in these models. The high-density model, ρ_{CO_2} = 750 kg/m^3, was able to account for almost 82% of the known injected mass. From the reservoir simulation models, we expect about 17% dissolution into aquifer water for the high-density case, for a total of 99% of the injected mass. However, if the CO_2 in the aquifer is in the low-density state, with ρ_{CO_2} = 550 kg/m^3, the seismic model accounts for only about 60% of the injected mass, assuming a uniform distribution for the diffuse CO_2. Reservoir simulations indicate that just less than 23% dissolution of CO_2 into water would occur, thus accounting for only about 83% of the injected mass. This leaves 17% of the mass unaccounted for in both 1999 and 2001.

It is useful to revisit the low-density gravity model calculated from the seismic data in terms of a patchy CO_2 volume. It is a straightforward exercise to imagine putting the missing 17% back into the diffuse volume and redistributing the volume in such a way that the pushdown constraint is satisfied. From Table 5-3 it is apparent that (in view of the maximum gravity predicted) the diffuse volume of CO_2 accounts for 8.0 μGal/MT in 1999 and about 7.6 μGal/MT in 2001. Putting the missing 17% of the injected CO_2 mass back into the model each year at the rates above adds 3.2 μGal to the maximum gravity in 1999 and 5.5 μGal in 2001.

This means that the expected change in the maximum gravity increases from 3.3 to 4.5 μGal/year.

Using this value means that the maximum gravity value predicted by the two types of models (seismic and reservoir simulation) have good agreement (Table 5-4). This indicates that the detailed geometry of the CO_2 bubble does not have a large effect on the observed peak gravity change. This insensitivity to detailed flow geometry suggests that the magnitude of the maximum time-lapse gravity signal will be due primarily to CO_2 density.

Model	ρ_{CO2} (kg/m^3)	Maximum change (μGal/year)
Seismic horizon	350	~7.4
Seismic horizon	550	4.5
Seismic horizon	700	2.7
Model I	700	2.2
Model IIa	700	2.4
Model IIb	550	4.7

The values given for the seismic horizon models with ρ_{CO2} = 350 kg/m^3 and ρ_{CO2} = 550 kg/m^3 are an estimate of the result of redistributing the diffuse CO_2 to match the pushdown and injected mass (see the text).

Table 5-4: Summary of the maximum magnitude of the gravity change expected per year for each of the different models.

As a final exercise, an extreme case in which the reservoir temperature is warmer than 45 °C can be examined. As the temperature increases, the average density of CO_2 within the reservoir decreases rapidly. Taking the average density of CO_2 as ρ_{CO_2} = 350 kg/m^3 and following the procedure outlined above, the expected gravity from the seismically imaged horizons can be calculated. The pushdown can be estimated using the velocity versus saturation from the 45 °C curve shown in Figure 5-4. This is not completely accurate and tends to under predict the mass of CO_2 by a few percent. However, this illustrates possible expectations for an extreme scenario. Tables 5-3 and 5-4 show the results of this calculation. The total mass estimated from the model is only 40% of the total injected mass. The contribution of the diffuse volume to gravity is about 17.8 μGal/MT in 1999 and 16.5 μGal/MT in 2001. Assuming a dissolution of 40% (a very large amount) and distributing the missing 20% of the injected mass into patchy saturation volume, the expected gravity change is to 7.4 μGal/year. For a 3-year time span, the maximum gravity change would be 22.2 μGal. With less dissolution of CO_2 the change in gravity could be even larger. This signal would be clearly discernable in the gravity data. In fact, assuming no dissolution gives a change of ~13 μGal/year applying the same logic. Comparing this to the feasibility study of Williamson et al. (2001), which predicted 15 μGal/year for ρ_{CO_2} = 350 kg/m^3 and no dissolution, it is again apparent that the detailed flow geometry will have minimal effect on the estimate of CO_2 density from gravity. To date, no reservoir simulation models have been calculated for temperatures higher than 45 °C, so the amount of CO_2 dissolution is speculation.

With a time span of 3 years, the expected maximum decrease in the observed gravity is between 7 and 14 μGal, depending on the density of CO_2 within the reservoir (Table 5-4). Figure 5-19 shows the observed gravity along with model predictions. Figure 5-19b shows the direct comparison between the measured gravity change and the gravity change predicted

from forward modeling. Only the benchmarks on the main line (SP01 through SP20) are shown. Although the maximum decrease in the time-lapse gravity is 15 ± 5.6 μGal, the scatter along the profile make it difficult to pick the best fitting model.

Figure 5-19a shows a spatially smoothed version of the forward model predictions and the observed gravity. The smoothing was done by averaging each point with its nearest neighbor to the east. Three points from about 2200 to 3200 m easting, which have smaller error bars, include the nearby points off the northwest–southeast trending main line, so that all the time-lapse gravity information is collapsed onto a single line. This reduces point to point scatter and makes it easier to discriminate areas of spatially correlated changes. The error bars for this plot were calculated as the time-lapse uncertainty (5.3 μGal) divided by the square root of the number of points included in the average. The difference in the shape of the reservoir models and seismic model reflects the differences between the CO_2 flow geometries. The flow in the idealized reservoir simulation models is simplified and has a much larger westward component than the seismic data indicate. The smoothed observations fit the high temperature seismic model the best, suggesting that the CO_2 has an average density near 550 kg/m^3 and that the extent of the CO_2 bubble is imaged accurately by reflection seismics.

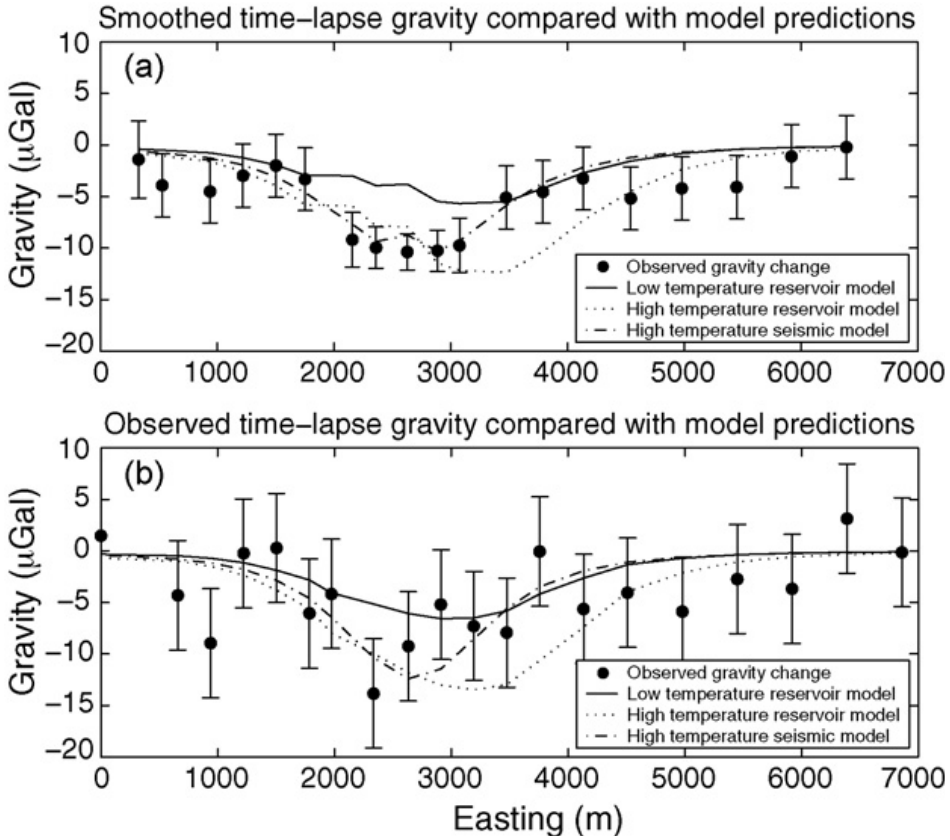

Figure 5-19: (a) Observed time-lapse gravity change plotted along with predicted gravity change for a high reservoir temperature (average CO_2 density of 550 kg/m^3) and a low reservoir temperature (average CO_2 density of 700 kg/m^3) models. Both the models and the observations have been smoothed by averaging neighboring values. (b) Time-lapse gravity with no smoothing for the 20 points on the main NE–SW trending line (benchmarks 1–20). In both plots, the observed gravity changes are most similar to the high temperature seismic model.

In order to characterize the density resolving power of this technique, a suite of models was constructed by linearly extrapolating the smoothed seismic forward models to other density values. This is justified since a simple linear scaling of the high-density model prediction matches the low-density model predictions. Model fit was determined by computing χ^2 for each density, where χ^2 is defined as

$$\chi^2 = \sum_{i=1}^{N} \frac{(\bar{g}_i - \bar{m}_i)^2}{\sigma_i^2}. \tag{5.5}$$

In equation 5.5, $\bar{g}_i$ is the ith smoothed time-lapse gravity value, $\bar{m}_i$ the ith smoothed model value, σ_i the uncertainty in the ith smoothed time-lapse gravity value, and $N = 19$ is the number of smoothed points. Figure 5-20 shows χ^2/N versus CO_2 density. The best estimate of in situ CO_2 density is 530 kg/m^3 with a 95% confidence interval of ±65 kg/m^3, shown by the shaded region. The 95% confidence interval indicates that if the experiment were repeated, 95% of the time the best fitting model would fall between 465 and 595 kg/m^3, based on our estimated uncertainties. This demonstrates the resolving power of this technique assuming there is uncertainty only in the gravity; however, there are unaccounted for uncertainties in the modeling, which arise from uncertainties in the seismic data, uncertainties in determining CO_2 saturation from seismic pushdown, and unknown flow geometry from 2002 to 2005. These modeling uncertainties are difficult to quantify. The difference between the seismic and reservoir simulation models gives an idea of the possible uncertainty in the modeling. The maximum difference between the two is about 1.5 μGal over 3 years. Another seismic survey is needed in order to constrain the flow geometry from 2002 to 2005 before firm conclusions can be drawn. Future gravity measurements will put better constraints on the CO_2 density and continue to map out the CO_2 flow.

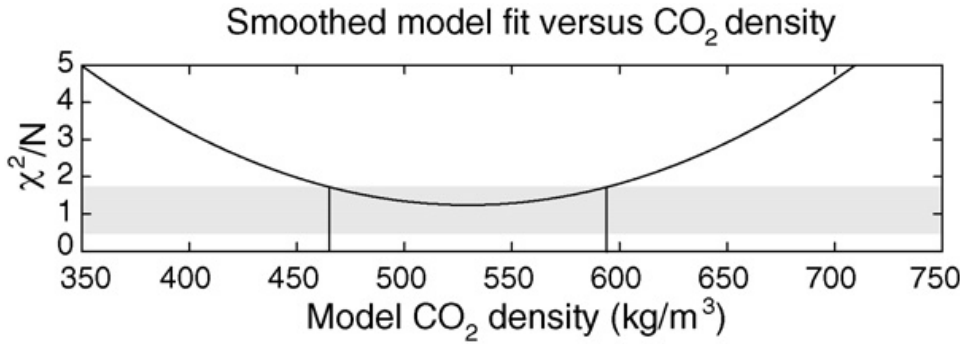

Figure 5-20: A suite of forward models was built by linearly extrapolating the gravity results from the smoothed seismic models. Model misfit (χ^2) normalized by the number of measurements ($N = 19$) is plotted against model CO_2 density for the smoothed seismic models. A minimum misfit occurs at a density of 530 kg/m^3 with a 95% confidence interval of ±65 kg/m^3. The 95% confidence interval is indicated by grey shading.

5.8 Conclusion

This study, has shown that it is possible to measure gravity on the seafloor with uncertainties of <5 μGal, even in a relatively shallow water, high noise environment. Additionally, is has been shown that by simultaneously measuring water pressure, seafloor depth can be determined to sub-centimeter accuracy, relative to a 'fixed' point on the seafloor. These depth measurements are very important for correcting the gravity measurements for anomalous changes in benchmark height, such as from sediment scouring. In the future at shallow high

current environments such as Sleipner, more care should be taken in designing and deploying benchmarks, in order to reduce the effects of scouring and biological disturbances. Techniques such as laying gravel or carpet down prior to benchmark emplacement, or anchoring the benchmarks to the seabed could be employed.

The time-lapse gravity results and modeling presented here support evidence from heat flow measurements and other temperature measurements in the vicinity of Sleipner which suggest the Utsira formation is warmer than previously thought. This is only a beginning step in characterizing the aquifer using time-lapse geophysical measurements. Additional gravity and seismic measurements are needed to further constrain this reservoir property by putting tighter bounds on the in situ CO_2 density. Ideally, future 3D seismic measurements and gravity measurements will be made within a few months of each other, so that the geometry of the CO_2 bubble determined from seismics will directly relate to observed changes in gravity.

Time-lapse gravimetric reservoir monitoring may play a role in future CO_2 sequestration efforts, however, this detection technique relies on the density contrast between injected CO_2 and the aquifer fluids, limiting its applicability to fluid filled reservoirs and excluding formations such as depleted coal beds. The best results will be obtained when monitoring shallow reservoirs less than 1000 m deep, where the density of CO_2 is much less than that of the reservoir fluids. In order to slow CO_2 emissions, as is needed to mitigate anthropogenic climate change, hundreds of sites such as Sleipner will be needed along with many other carbon reduction strategies. Undoubtedly, gravity will be a useful tool for monitoring injected CO_2 for a number of these sites.

Acknowledgements
Håvard Alnes provided invaluable assistance with the data processing code. We would also like to acknowledge the ship and ROV crew of the *Edda Freya* and the *Normand Mjolne* for their patience and careful treatment of the ROVDOG instruments.

Chapter 6

Monitoring both gas production and CO2 injection at the Sleipner field using time-lapse gravimetry

Is not included due to copyright

Chapter 7

Gravimetric monitoring of gas production from the Troll field

Is not included due to copyright

Chapter 8

Gravimetric monitoring of gas reservoir water influx-a combined flow- and gravity-modeling approach

Is not included due to copyright

9 Closing remarks

Due to steps taken as described in this thesis, the precision of the gravity surveys have improved from 26 μGal in the first survey to 3-5 μGal in the recent surveys. 3 μGal was achieved in surveys where the weather was excellent (Midgard and Mikkel 2006) while 5 μGal was achieved in surveys (Troll 2005, Snøhvit 2007) where the weather was marginal (3-5 m maximum waveheight persisted throughout large parts of the surveys, although for Snøhvit problems with the ROV were also significant). The stability of the ship and the robustness of the ROV (during launch and recovery) to bad weather, as well as the skills of the ROV pilots, are also important factors. Bad weather is likely to cause rougher instrument handling and a less continuous operation, leading to less similar temperature and transport exposures between measurements. Such exposures and delays are likely to increase gravimeter drift errors and reduce the gravity repeatability.

The time-lapse station uncertainty depends to a large degree on the number of visits afforded on each station in each survey. The time-lapse results between 2002 and 2005 for Troll and Sleipner illustrate this: for Troll, where 70-80 % of the stations were visited only once in the two surveys, the time-lapse uncertainty is 6.5 μGal; while for Sleipner, where all stations were visited 2-3 times in each survey, the time-lapse uncertainty is 3.6 μGal (Table 4-2). The single-station uncertainty on Sleipner of 3.6 μGal can be put in perspective by relating it to a GWC rise: in the 1D limit (equation 8.2) for a bulk density change of 100 kg/m^3 (quite typical for water displacing gas) it corresponds to a thickness (or GWC rise) of 0.9 m; for a cylinder model of radius equal to cylinder/reservoir depth, 3.6 μGal corresponds to a thickness of 2.9 m (Chapter 8.3, equation 8.1). For a cylinder radius half the reservoir depth, 3.6 μGal corresponds to a GWC rise of 8.1 m, which is quite similar to the detection threshold of 4D seismic at Sleipner Øst of 9 m (Alsos et al. 2003; Eiken et al. 2005). In terms of minimum water volume using the point-mass formula (equation 1.1) and $\Delta\rho_f$ = 850 kg/m^3, 3.6 μGal corresponds to a water volume of 0.65 $\times 10^6$ m^3 for a reservoir depth of 1000 m, and for a depth of 2000 m the water volume is 2.6 $\times 10^6$ m^3.

Regarding the TL-gravity results, I find the Ty response as seen in Figure 6-6 to be an excellent example of the power of time-lapse gravity in detecting and quantifying water influx. With a peak gravity change from the profile of about 35 μGal, we can by use of the minimum water influx formula (equation 1.1), a reservoir depth of 2.3 km, and a density contrast between water and gas of 850 kg/m^3, roughly estimate the minimum required water influx volume to 33 $\times 10^6$ m^3. Since this is the minimum model, the true water influx volume is somewhat larger. However, the point is that a powerful constraint on the simulation model regarding the speed and magnitude of water influx is established from a practically single profile covering only a small part of the anomaly. It is also noteworthy that a nearly similar result was available just a few weeks after the Sleipner 2005 survey ended; i.e. the reprocessing and new available data that proved important for the CO_2 density estimate (Chapter 6), had negligible impact on the magnitude of the extracted Ty-response with its about ten times higher amplitude. In comparison, seismic takes months to process and can be complicated to interpret, and if there is shortage on trained people for doing the specialized 4D interpretation, we can soon talk about a year or more.

Gravimetric monitoring can in my opinion offer obvious aids to the management of possible water-drive gas reservoirs (Chapter 8). First, it may be used at a relatively early stage (determined from feasibility study) to unambiguously determine whether there is significant

water influx or not. If not, it may be unnecessary to continue the monitoring program, unless subsidence or depletion is feasible to monitor from the subsidence and gravity measurements. If there is a significant waterdrive, the magnitude and distribution of incoming water is of interest to monitor because of the potential importance for gas production and recovery. If a lateral resolution significantly better than the reservoir depth is required e.g. to detect thief zones, 4D seismic may be used. Of course thief zones are much less likely to occur if water displaces gas than vice versa due to their difference in fluid mobility. Seismic and gravimetry may also be used together, as the gravity method offers complementary density change information (Chapter 1). One may alternatively use time-lapse gravimetry to determine when to collect the more expensive (per survey) 4D seismic.

To continue the improvement of gravity accuracy is important for several reasons: it will make the method more cost efficient (need fewer repeats to obtain a given accuracy), it will enable monitoring of fields with smaller gravity changes (deeper reservoirs, smaller reservoirs, and smaller density changes), and it will enable more frequent monitoring. Currently instrumental drift is the largest error and recovery (short term drift during measurements) is the second largest error of the gravity method. While recovery appears to be most sensitive to instrument handling (certainly it is sensitive to instrument tilt), the instrumental drift is dependent on both handling and ambient temperature changes. Possible approaches (in random order) to reduce drift errors are (1) to make more frequent repeats to avoid aliasing if the drift varies (requires on-board decisions and quality control of measurements), (2) to find better ways to correct the drift by improved understanding of its causes, (3) to better shield the instrument from ambient temperature changes and shocks, and (4) to reduce the ambient temperature changes and shocks. Regarding (2), one possibility that appears attractive is if we could incorporate the temperature history (ambient and internal temperatures) to better determine survey drift. Gerstenecker (1981) built a model for the Lacoste-Romberg gravimeter based on experiments and the use of system control theory; his model showed the connection between temperature induced drift and temperature via a convolution integral. However, this method appears not to be used for correcting gravimeter drift in practice; Becker (1984) stated that the complexity of the method (e.g. the superposition of adiabatic effects) combined with the sensitiveness of the gravimeter to biased temperature influences made it questionable if it would improve the accuracy in the field, and that shielding the gravimeter from temperature variations by a thermoregulated external box appeared to be a better approach.

Experiments and analysis of survey data are currently on-going to address, in particular, the errors caused by drift and recovery. Hopefully the repeatability can be stabilized below 3 μGal, and the outcome of the ongoing experiments may show whether intra-survey repeatability below 2 μGal will be possible in the near future

.

References

Absolute Pressure Transducers. Series 3000 and 4000. 1997. Paroscientific, Inc., Digiquartz Pressure Instrumentation, www.paroscientific.com.

Agarwal, R. G., R. Al-Hussainy, and H. J. Ramey, 1965, The importance of water influx in Gas reservoirs: Journal of Petroleum Technology, 17, 1336-1342.

Agnew, D. C., 1996, SPOTL: Some programs for ocean-tide loading, SIO Reference Series 96-8, Scripps Institution of Oceanography.

Agnew, D. C., 1997, NLOADF: a program for computing ocean-tide loading, Journal of Geophysical Research, 102, 5109-5110.

Allis, R. G., and T. M. Hunt, 1996, Analysis of exploitation-induced gravity changes at Wairakei geothermal field: Geophysics, 51, 1647–1660.

Alsos, T., R. Tøndel, F. Aanvik, and O. A. solheim, 2003, Quantifying rise in gas water contact from time-lapse seismic on the Sleipner Øst field: EAGE Annual Meeting Abstract A-08.

Arts, R., R. A. Chadwick, O. Eiken, S. Thibeau, and S. L. Nooner, 2008, Ten years' experience of monitoring CO2 injection in the Utsira Sand at Sleipner, offshore Norway: First Break, 26, 29-36.

Arts, R., R. Elsayed, L. van der Meer, O. Eiken, S. Østmo, A. Chadwick, G. Kirby, and B. Zinszner, 2002, Estimation of the mass of injected CO2 at Sleipner using time-lapse seismic data: Paper presented at EAGE, Annual Meeting, Florence, Italy.

Arts, R., O. Eiken, A. Chadwick, P. Zweigel, L. van der Meer, and B. Zinszner, 2003, Monitoring of CO2 injected at Sleipner using time lapse seismic data: Paper presented at Abstracts of the Sixth International Conference on Greenhouse Gas Control Technology (GHGT-6), Kyoto, Japan, October 1–4, 2002.

Babcock, J. M., B. A. Kirkendall, and J. A. Orcutt, 1994, Relationships between ocean bottom noise and the environment: Bull. Seis. Soc. Am., 84, 1991–2007.

Ballu, V., J. Dubois, G. C. Deplus, M. Diament, and S. Bonvalot, 1998, Crustal structure of the Mid -Atlantic Ridge south of the Kane fracture zone from seafloor and sea surface gravity data: Journal of Geophysical Research, 103, 2615–2631.

Becker, M., 1984, Analyse von hochpräzisen Schweremessungen: Deutsche Geodätische Kommisson, der Bayerischen Akademie der Wissenschaften, Reihe C, Dissertationen, No 294.

Berrino, G., G. Corrado, U. Riccardi, 2006, On the capability of recording gravity stations to detect signals coming from volcanic activity: The case of Vesuvius: Journal of Volcanology and Geothermal Research, 150, 270-282.

Blackman, D. K., J. R. Cann, B. Janssen, and D. K. Smith, 1998, Origin of extensional core complexes: Evidence from the Mid-Atlantic Ridge at Atlantis fracture zone: Journal of Geophysical Research, 103, 21315–21334.

Blakely, R. J., 1996, Potential theory in gravity and magnetic applications: Cambridge University Press.

Bonvalot, S., M. Diament, and G. Gabalda, 1998, Continuous gravity recording with Scintrex CG-3M meters: A promising tool for monitoring active zones: Geophysical Journal International, 135, 470–494.

Brady, J. L, J. F. Ferguson, J. E. Seibert, T. Chen, J. L. Hare, C. V. L. Aiken, F. J. Klopping, and J. M. Brown, 2004, Surface-gravity monitoring of the gas cap water injection project, Prudhoe Bay, Alaska: SPE Reservoir Evaluation & Engineering, 7, 59–67.

Brown, A. R., 2004, Interpretation of three-dimensional seismic data, sixth edition: The American Association of Petroleum Geologists and the Society of Exploration Geophysicists.

Bruno, M. S. 1992. Subsidence-Induced Well Failure: SPE Drilling Engineering*,* 7**,** 148–152.

Bruno, M. S., 2002, Geomechanical and decision analyses for mitigating compaction-related casing damage: SPE Drilling and Completion, September, 179-188.

Bruns, J. R., M. J. Fetkovich, and V. C. Meitzen, 1965, The effect of water influx on p/z-cumulative gas production curves: Journal of Petroleum Technology, 17, 287-291.

Carbone, D., and H. Rymer, 1999, Calibration shifts in a LaCoste-and-Romberg gravimeter: Comparison with a Scintrex CG-3M, Geophysical Prospecting, 47, 73-83.

Carbone, D., G. Budetta, F. Greco, and H. Rymer, 2003, Combined discrete and continuous gravity observations at Mount Etna: Journal of Volcanology and Geothermal Research, 123, 123-135.

Cason, L. D., 1989, Water flooding increases gas recovery, Journal of Petroleum Technology, 41, 1102-1106.

Chadwick, R. A., S. Holloway, G. A. Kirby, U. Gregersen, and P. N. Johannessen, 2000, The Utsira Sand, Central North Sea—An assessment of its potential for regional disposal: In The 5th International Conference on Greenhouse Gas Control Technologies, Cairns, Australia.

Chadwick, R. A., R. Arts, O. Eiken, G. A. Kirby, E. Lindeberge, and P. Zweigel, 2004, 4D seismic imaging of an injected CO2 plume at the Sleipner Field, central North Sea: In 3D Seismic Technology, edited by R.J. Davies, J.A. Cartwright, S.A. Stewart, M. Lappin, and J.R. Underhill, Geological Society of London.

Chadwick, R. A., R. Arts, and O. Eiken, 2005, 4D seismic quantification of a growing CO2 plume at Sleipner, North Sea: In: Dore, A.G. and B. A. Vining, (eds.), Petroleum Geology: North-West Europe and Global Perspectives – Proceedings of the 6th Petroleum Geology Conference, 1385-1399.

Chadwick, W. W. Jr., S. L. Nooner, M. A. Zumberge, R. W. Embley, and C. G. Fox, 2006, Vertical deformation monitoring at Axial Seamount since its 1998 eruption using deep-sea pressure sensors: Journal of Volcanology and Geothermal Research, 150, 313-327.

Chin, L. Y. and N. B. Nagel, 2004, Modeling of subsidence and reservoir compaction under waterflood operations: International Journal of Geomechanics, March, 28-34.

Cochran, J. R., B. J. Coakley, D. J. Fornari, and R. E. Herr, 1994, Continuous underway near-bottom gravity measurements from a submersible: EOS, Transactions, American Geophysical Union, 75, 579.

Collins, J. A., F. L. Vernon, J. A. Orcutt, R. A. Stephen, K. R. Peal, F. B. Wooding, F. N. Spiess, and J. A. Hildebrand, 2001, Broadband seismology in the oceans: Lessons from the Ocean Seismic Network pilot experiment: Geophysical Research Letters, 28, 49–52.

Craig, F. F., 1971, The reservoir engineering aspects of waterflooding: SPE Monograph Vol. 3, 1993.

Dake, L. P., 1978, Fundamentals of reservoir engineering: Elsevier.

Dake, L. P., 2001, The practice of reservoir engineering (Revised Edition): Elsevier.

Dampney, C. N. G., 1969, The equivalent source technique: Geophysics, 34, 39-53.

Davis, E., C. Wright, S. Demetrius, J. Choi, and G. Galey, 2000, Precise Tiltmeter Subsidence Monitoring Enhances Reservoir Management: Paper SPE 62577.

Du, J. and J. E. Olson, 2001, a poroelastic reservoir model for predicting subsidence and mapping subsurface pressure fronts: Journal of Petroleum Science and Engineering, 30, 181-197.

Eble, M. C. and F. I. Gonzalez, 1990, Deep-Ocean Bottom Pressure Measurements in the Northeast Pacific: Tsunami Project, PMEL, NOAA Report 1196.

Egbert, G. D., A. F. Bennett, and M. G. G. Foreman, 1994, TOPEX/POSEIDON tides estimated using a global inverse model. Journal of Geophysical Research, 99, 821-824.

Eikeland; K.M. and H. Hansen, 2007, Dry-Gas Reinjection in a Strong Waterdrive Gas-Condensate Field Increases Condensate Recovery – Case Study: The Sleipner Ty Field, South Viking Graben, Norwegian North Sea: Paper SPE 110309.

Eiken, O., M. A. Zumberge, and G. S. Sasagawa, 2000, Gravity monitoring of offshore gas reservoirs: 70th Annual International Meeting, SEG, Expanded Abstracts, 431–434.

Eiken, O., M. Zumberge, and J. Hildebrand, 2003, A method for monitoring seafloor subsidence and for gravity monitoring an underground hydrocarbon reservoir. Den Norske Stats Oljeselskap A. S. and The Regents of the University of California. UK Patent No. 2 377 500, and US Patent No. 6 813 564.

Eiken, O., M. A. Zumberge, T. Stenvold, G. S. Sasagawa, and S. Nooner, 2004, Gravimetric monitoring of gas production from the Troll field: 74th Annual International Meeting, SEG, Expanded Abstracts, 2243–2246.

Eiken, O., T. Tollefsen, F. Aanvik, and T. Alsos, 2005, Surface geophysical monitoring of gas fields: some experiences: In: Dore, A.G. and Vining, B.A. (eds.), Petroleum Geology: North-West Europe and Global Perspectives – Proceedings of the 6th Petroleum Geology Conference, 641-650.

Eiken, O. and R. Tøndel, 2005, Sensitivity of time-lapse seismic data to pore pressure changes: Is quantification possible?: The Leading Edge, 24, 1250-1254.

Evans, R. L., 1996, A seafloor gravity profile across the TAG hydrothermal mound: Geophysical Research Letters, 23, 3447–3450.

Fetkovich, M. J., D. E. Reese, and C. H. Whitson, 1998, Application of a general material balance for high-pressure gas reservoirs: SPE Journal, 3, 3–13.

Ferguson, J. F, T. Chen, J. Brady, C. L. V. Aiken, and J. Seibert, 2007, The 4D microgravity method for waterflood surveillance: Part II – Gravity measurements for the Prudhoe Bay reservoir, Alaska: Geophysics, 72, no. 2, I33-I43.

Fjær, E., R. M. Holt, P. Hornsrud, A. M. Raaen, and R. Risnes, 2008, Petroleum related rock mechanics, 2nd ed.: Elsevier.

Fokker, P. A., 2002, Subsidence prediction and inversion of subsidence data: Paper SPE 78227.

Foster, D. G., 2008, Lessons learned from over 20 years of 4-D deployment: Paper SPE 113542.

Geertsma, J., 1973, Land Subsidence above Compacting Oil and Gas Reservoirs. JPT, 25, 734–744.

Gerstenecker, C., 1981, A model for studying temperature effects on Lacoste-Romberg gravimeters: Bulletin D'Information – Bureau Gravimetrique International, 49, 64-71.

Gray, D. I. 1987, Troll: In: Spencer, A. M. et al. (eds.) Geology of the Norwegian Oil and Gas Fields, 389-401.

Gutierrez, M. and R. W. Lewis, 1998, The Role of Geomechanics in Reservoir Simulation: Paper SPE 47392.

Hammer, S., 1945, Estimating ore masses in gravity prospecting: Geophysics, 10, 50-62.

Hammerstad, E., 1997, Multibeam Echo Sounder for EEZ Mapping: OCEANS MTS/IEEE Conference Proceedings 1216–1221.

Han, D., M. L. Batzle, 2004, Gassmann's equation and fluid saturation effects on seismic velocities: Geophysics 69, 398– 405.

Hansen, H., and K. Westvik, 2000, Successful multidisciplinary teamwork increases income. Case study: The Sleipner East Ty Field, South Viking Graben, North Sea: Paper SPE 65135.

Hansen, H., O. Eiken, and T. O. Aasum, 2005, Tracing the Path of Carbon Dioxide From a Gas/Condensate Reservoir, Through an Amine Plant and Back Into a Subsurface Aquifer – Case Study: The Sleipner Area, Norwegian North Sea: Paper SPE 96742.

Hansen, P. C., 1998, Rank-deficient and discrete ill-posed problems. Numerical aspects of linear inversion: Society for Industrial and Applied Mathematics.

Hare J. L., J. F. Ferguson, C. L. V. Aiken and J. L. Brady, 1999, The 4-D microgravity method for waterflood surveillance: A model study for the Prudhoe Bay reservoir, Alaska: Geophysics, 64, 78–87.

Heerten, G., 1981, Experiences of different scour protection techniques at offshore-structures in the North Sea: In: Paper Presented at Fifth Australian Conference on Coastal and Ocean Engineering, 135-136.

Hermanrud, C., 1988, Determination of formation temperature from downhole measurements: Ph.D. thesis. University of South Carolina, Columbia, SC.

Hettema, M., E. Papamichos, and P. Schutjens, 2002, Subsidence Delay: Field Observations and Analysis: Oil & Gas Science and Technology, 57, 443–458.

Hildebrand, J. A., J.M. Stevenson, P. T. C. Hammer, M. A. Zumberge, R. L. Parker, C. G. Fox, and P- J. Meis, 1990, A seafloor and sea surface gravity survey of Axial Volcano: Journal of Geophysical Research, 95, 12751–12763.

Holmes, M. L., and H. P. Johnson, 1993, Upper crustal densities derived from sea floor gravity measurements; northern Juan de Fuca Ridge: Geophysical Research Letters, 20, 1871–1874.

Holloway, S., R. A. Chadwick, G. A. Kirby, J. M. Pearce, U. Gregersen, P.N. Johannessen, L. Kristensen, P. Zweigel, and R. Arts, 2000, Work Area 1 (Geology), in Saline Aquifer CO2 Storage (SACS)—Final report.

Holt, R. M., M. Brignol, E. Fjaer, T. Erling, and C. J. Kenter, 1994, Core Damage Effects on Compaction Behavior: Paper SPE 28027.

Houston, M. H. and Paros, J. M. 1988. High Accuracy Pressure Instrumentation for Underwater Applications. Paper presented at the IEEE Intl. Symposium on Underwater Technology, Tokyo, 15–17 April.

Hunt, T. M., 1970, Net mass loss from the Wairakei geothermal field, New Zealand: Geothermics, 2, 487–491.

Hunt, T. M. and W. M. Kissling, 1994, Determination of reservoir properties at Wairakei geothermal field using gravity change measurements: Journal of Volcanology and Geothermal Research, 63, 129-143.

Johnson, J. W., and J. J. Nitao, 2003, Reactive transport modelling of geologic CO2 sequestration at Sleipner: in Greenhouse Gas Control Technologies, edited by J. Gale, and Y. Kaya, pp. 327-332, Elsevier Science Ltd.

Klins, M. A., A. J. Bouchard, and C. L. Cable, 1988, A polynomial approach to the van Everdingen-Hurst dimensionless variables for water encroachment: SPE Reservoir Engineering, 3, 320–326.

LaCoste, L., 1967, Measurement of gravity at sea and in the air: Reviews of Geophysics, 5, 477–526.

Lambert, A., N. Courtier, G. S. Sasagawa, F. Klopping, D. Winester, T. S. James, and J. O. Liard, 2001, New constraints on Laurentide postglacial rebound from absolute gravity measurements, Geophysical Research Letters, 28, 2109-2112.

Landrø, M., O. A. Solheim, E. Hilde, B. O. Ekren, and L. K. Strønen, 1999, The Gullfaks 4D seismic study: Petroleum Geoscience, 5, 213-226.

Leäo, J. W. D. and J. B. C. Silva, 1989, Discrete linear transformations of potential field data: Geophysics, 54, 497-507.
Lighthill, J., 1978, Waves in Fluids: Cambridge University Press.
Lindeberg, E., B. van der Meer, A. Moen, D. Wessel-Berg, and A. Ghaderi, 2000, Work Area 2 (Reservoir): in Saline Aquifer CO2 Storage (SACS)—Final report, 2000.
Lindeberg, E. and P. Bergmo, 2003, The long-term fate of CO2 injected into an aquifer, in J. Gale and Y. Kaya, eds., 6th conference on Greenhouse Gas Control Technologies, 489-495.
Lindsey, J. P., 1989, The Fresnel zone and its interpretive significance: The Leading Edge, 8, 33-39.
Jack, I, 1997, Time-lapse seismic in reservoir management: Society of Exploration Geophysicists.
Longuet-Higgins, M.S., 1950, A theory of the origin of microseisms: Philisophical Transactions of the Royal Society of London, A234, 1-35.
Lyness, D., 1985, The gravimetric detection of mining subsidence: Geophysical Prospecting, 33, 567-576.
Macini, P. and E. Mesini, 2002, Radioactive marker technique applications to evaluate compaction in environmentally sensitive areas: Paper SPE 74411.
Marchina, P. J. M, 1996, The use of subsidence data to monitor reservoir behavior: Paper SPE 36918.
Mattax, C. C. and R. L. Dalton, 1990, Reservoir simulation: SPE Monograph Series, Volume 13.
Mavko, G., and T. Mukerji, 1998, Bounds on low-frequency seismic velocities in partially saturated rocks: Geophysics, 63, 918– 924.
McCain, W. D., 1990, The properties of petroleum fluids, 2nd ed.: PennWell Publishing Company.
McCain, W. D., 1991, Reservoir-fluid property correlations—state of the art: SPE Reservoir Engineering, 6, 266–272.
Merle, H. A, C. J. P. Kentie, G. H. C. van Opstal, and G. M. G. Schneider, 1976, The Bachaquero Study—A Composite Analysis of the Behavior of a Compaction Drive/Solution Gas Drive Reservoir: Journal of Petroleum Technology, 28, 1107–1115.
Mes, M. J., 1991, Accuracy of Offshore Subsidence Measurements With Seabed Pressure Gauges: SPEFE, 6**,** 463–469.
Mes, M. J., H. Landau, and C. Luttenberger, 1996, Ekofisk Automatic GPS Subsidence Measurements: Sea Technology, 37, 15–22.
Mjøen, K., 1988, Bassengmodellering - termiske effekter av Pliocene/Pleistocene nedisinger: Diploma thesis. Norges Tekniske Høgskole, Trondheim, Norway.
Morita, N., D. L. Whitfill, O. Nygaard, and A. Bale, 1989, A quick method to determine subsidence, reservoir compaction, and in-situ stress induced by reservoir depletion: Journal of Petroleum Technology, 41, 71-84.
Nagel, N. B., 1998, Ekofisk Field Overburden Modelling: Paper SPE 47345.
Nolen-Hoeksema, R.C., 2000, Modulus-porosity relations, Gassmann's equations, and the low-frequency elastic-wave response to fluids: Geophysics, 65, 1355–1363.
Nooner, S. L. 2005, Gravity changes associated with underground injection of CO2 at the Sleipner storage reservoir in the North Sea, and other marine geodetic studies: PhD dissertation. University of California, San Diego.
Nooner, S. L., O. Eiken, C. Hermanrud, G. S. Sasagawa, T. Stenvold, and M. S. Zumberge, 2007, Constraints on the in situ density of CO2 within the Utsira formation from

time-lapse seafloor gravity measurements: International Journal of Greenhouse Gas Control, 1, 198-214.
Nooner, S. L., M. A. Zumberge, O. Eiken, T. Stenvold and G.S. Sasagawa, 2003, Seafloor micro-gravity survey of the Sleipner CO2 sequestration site: EOS Transactions, AGU, 84(46), Fall Meet. Suppl., Abstract GC31A-01.
Nooner, S., et al., 2004. A baseline seafloor gravity survey over the Sleipner CO2 sequestration site. In: Paper Presented at Third Annual Carbon Capture and Sequestration Proceedings. Exchange Monitor Publications, Washington, DC.
Nordquist, G, J. A. P Protacio, J. A. Acuña, 2004, Precision gravity monitoring of the Bulalo geothermal field, Philippines: independent checks and constraints on numerical simulation: Geothermics, 33, 37-56.
Parker, R. L., 1977, Understanbding inverse theory: Ann. Rev. Earth Planet. Sci., 5, 35-64.
Rider, M. H., 1986, The Geological Interpretation of Well Logs: Blackie and Son Limited.
Roy, A., 1962, Ambiguity in geophysical interpretation: Geophysics, 27, 90-99.
Rymer, H., 1994: Microgravity change as a precursor to volcanic activity: Journal of Volcanology and Geothermal Research, 61, 311-328.
San Andres, R. B. and J. R. Pedersen, 1993, Monitoring the Bulalo geothermal reservoir, Philippines, using precision gravity data: Geothermics, 22, 395-402.
Sasagawa, G. S., M. A. Zumberge, J. M. Stevenson, T. Lautzenhiser, J. Wirtz, and M. E. Ander, 1989, The 1987 southeastern Alaska gravity calibration range: Absolute and relative gravity: Journal of Geophysical Research, 94, 7661–7666.
Sasagawa, G. S., W. Crawford, O. Eiken, S. Nooner, T. Stenvold, and M. A. Zumberge, 2003, A new sea-floor gravimeter: Geophysics, 68, 544–553.
Segawa, J., and H. Fujimoto, 1988, Observation of an ocean bottom station installed in the Sagami Bay and replacement of the acoustic transponder attached to it: JAMSTECTR Deep Sea Research, 256, 251–257 (in Japanese).
Seigel, H. O., I. Brcic, and P. Mistry, 1993, The CG-3M – A high precision, microGal resolution, land gravimeter, with worldwide range: Internal Report, Scintrex Limited, Canada.
Sheldon, J. W. and F. J. Fayers, 1962, The motion of an interface between two fluids in a slightly dipping porous medium: SPE Journal, 2, 275–282.
Singh, B., and D. Guptasarma, 2001, New method for fast computation of gravity and magnetic anomalies from arbitrary polyhedra: Geophysics, 66, 521-526.
Skeels, D. C., 1947, Ambiguity in gravity interpretation: Geophysics, 12, 43-56.
Soulsby, R., 1998, Dynamics of Marine Sands: Thomas Telford Ltd., 272 pp.
Span, R., and W. Wagner, 1996, A new equation of state for carbon dioxide covering the fluid region from the triple-point to 1100 K at pressures up to 800 MPa: Journal of Physical and Chemical Reference Data, 25 (6).
Stark, P. B. and R. L. Parker, 1995, Bounded-variable least-squares: An algorithm and applications: Computational Statistics, 129-141.
Stenvold, T., O. Eiken, M. A. Zumberge, G. S. Sasagawa, and S. L. Nooner, 2006, High-precision relative depth and subsidence mapping from seafloor water pressure measurements: SPE Journal, 11, 380–389.
Sumer, M., Fredsoe, J., 2002, The Mechanics of Scour in the Marine Environment: World Scientific Publishing Co., 550 pp.
Telford, W. M., L. P. Geldart, and R. E. Sheriff, 1990, Applied geophysics, 2nd ed.: Cambridge University Press.
Torge, W., 1989, Gravimetry: Walter de Gruyter.
Van Gelderen, M., R. Haagermans, and M. Bilker, 1999, Gravity changes and natural gas extraction in Groningen: Geophysical Prospecting, 57, 979–993.

Vasco, D. W., K. Karasaki, and C. Doughty, 2000, Using surface deformation to image reservoir dynamics: Geophysics, 65, 132-146.

Vasco, D. W., C. Wicks, K. Karasaki, and O. Marques, 2002, Geodetic imaging: reservoir monitoring using satellite interferometry: Geophysical Journal International, 149, 555-571.

Vasco, D. W. and A. Feretti, 2005, On the use of quasi-static deformation to understand reservoir fluid flow: Geophysics, 70, no. 4, O13-O27.

Vennard, J. K., and R. L. Street, 1982, Elementary fluid mechanics: Wiley & Sons.

Wang, H. F., 2000, Theory of Linear Poroelasticity with Applications to Geomechanics and Hydrogeology: Princeton University Press.

Wang, Z., M. E. Cates, and R. L Langan, 1998, Seismic monitoring of a CO2 flood in a carbonate reservoir: a rock physics study: Geophysics 63, 1604–1617.

Water Level Recorders WLR 7 & WLR 8. 2000. Data Sheet D 196. Aanderaa Instruments, www.aanderaa.com.

Wearn, R. B. Jr. and N. G. Larson, 1982, Measurements of the sensitivities and drift of Digiquartz pressure sensors: Deep-Sea Research, 29, 111–134.

Whitehouse, R., 1998, Scour at Marine Structures: A Manual for Practical Applications: Thomas Telford Ltd., 198 pp.

Whitson, C. H. and M. R. Brulé, 2000, Phase behavior: SPE Monograph Vol. 20.

Willhite, 1986, Waterflooding: SPE textbook series Vol. 3.

Williams-Jones, G. and H. Rymer, 2002, Detecting volcanic eruption precursors: a new method using gravity and deformation measurements: Journal of Volcanology and Geothermal Research, 113, 379-389.

Williamson, J. P., R. A. Chadwick, W. J. Rowley, and O. Eiken, 2001, Work Area 5 (Geophysics) - Gravity monitoring of the CO2 bubble: in SACS-Saline Aquifer CO2 Storage Phase 2 (SACS2), British Geological Survey, Natural Environment Research Council.

Wyatt, F., R. Bilham, R. J. Beavan, A. G. Sylvester, T. Owen, A. Harvey, C. Macdonald, D. Jackson, and D. C. Agnew, 1984, Comparing tiltmeters for use in crustal deformation measurements: a preliminary report, Geophysical Research Letters, 11, 963-966.

Xu, H., and A. Nur, 2001, Integrating reservoir engineering and satellite remote sensing for (true) continuous time-lapse reservoir monitoring: The Leading Edge, 20, 1176-1179, 1198.

Zumberge, M. A., and E. L. Canuteson, 1995, An ocean bottom absolute gravity meter, Gravity and Geoid: Joint Symposium of the International Gravity Commission and the International Geoid Commission, Graz, Austria, September 11-17, 1994. Edited by Hans Sünkel and Iginio Marson. Berlin, New York: Springer, p.7.

Zweigel, P., R. Arts, A. Lothe, and E. Lindeberg, 2004, Reservoir geology of the Utsira Formation at the first industrial-scale underground CO2 storage site (Sleipner area, North Sea): in Geological Storage of Carbon Dioxide, edited by S. J. Baines, and R. H. Worden, Geological Society of London.